EUROPEAN ORGANISATION FOR NUCLEAR RESEARCH (CERN)

Measurements of $\pi^{\pm}$, $K^{\pm}$, p and $\bar{p}$ spectra in ^{7}Be+^{9}Be collisions at beam momenta from 19A to 150A GeV/c with the NA61/SHINE spectrometer at the CERN SPS

The NA61/SHINE Collaboration

The NA61/SHINE experiment at the CERN Super Proton Synchrotron (SPS) studies the onset of deconfinement in hadron matter by a scan of particle production in collisions of nuclei with various sizes at a set of energies covering the SPS energy range. This paper presents results on inclusive double-differential spectra, transverse momentum and rapidity distributions and mean multiplicities of $\pi^{\pm}$, $K^{\pm}$, p and $\bar{p}$ produced in the 20% most *central* ^{7}Be+^{9}Be collisions at beam momenta of 19A, 30A, 40A, 75A and 150A GeV/c. The energy dependence of the $K^{\pm}/\pi^{\pm}$ ratios as well as of inverse slope parameters of the $K^{\pm}$ transverse mass distributions are close to those found in inelastic p+p reactions. The new results are compared to the world data on p+p and Pb+Pb collisions as well as to predictions of the EPOS, UrQMD, AMPT, PHSD and SMASH models.

The NA61/SHINE Collaboration

A. Acharya[9], H. Adhikary[9], A. Aduszkiewicz[15], K.K. Allison[25], E.V. Andronov[21], T. Antićić[3], V. Babkin[19], M. Baszczyk[13], S. Bhosale[10], A. Blondel[4], M. Bogomilov[2], A. Brandin[20], A. Bravar[23], W. Bryliński[17], J. Brzychczyk[12], M. Buryakov[19], O. Busygina[18], A. Bzdak[13], H. Cherif[6], M. Ćirković[22], M. Csanad[7], J. Cybowska[17], T. Czopowicz[9,17], A. Damyanova[23], N. Davis[10], M. Deliyergiyev[9], M. Deveaux[6], A. Dmitriev[19], W. Dominik[15], P. Dorosz[13], J. Dumarchez[4], R. Engel[5], G.A. Feofilov[21], L. Fields[24], Z. Fodor[7,16], A. Garibov[1], M. Gaździcki[6,9], O. Golosov[20], V. Golovatyuk[19], M. Golubeva[18], K. Grebieszkow[17], F. Guber[18], A. Haesler[23], S.N. Igolkin[21], S. Ilieva[2], A. Ivashkin[18], S.R. Johnson[25], K. Kadija[3], N. Kargin[20], E. Kashirin[20], M. Kiełbowicz[10], V.A. Kireyeu[19], V. Klochkov[6], V.I. Kolesnikov[19], D. Kolev[2], A. Korzenev[23], V.N. Kovalenko[21], S. Kowalski[14], M. Koziel[6], B. Kozłowski[17], A. Krasnoperov[19], W. Kucewicz[13], M. Kuich[15], A. Kurepin[18], D. Larsen[12], A. László[7], T.V. Lazareva[21], M. Lewicki[16], K. Łojek[12], V.V. Lyubushkin[19], M. Maćkowiak-Pawłowska[17], Z. Majka[12], B. Maksiak[11], A.I. Malakhov[19], A. Marcinek[10], A.D. Marino[25], K. Marton[7], H.-J. Mathes[5], T. Matulewicz[15], V. Matveev[19], G.L. Melkumov[19], A.O. Merzlaya[12], B. Messerly[26], Ł. Mik[13], S. Morozov[18,20], S. Mrówczyński[9], Y. Nagai[25], M. Naskręt[16], V. Ozvenchuk[10], V. Paolone[26], O. Petukhov[18], R. Płaneta[12], P. Podlaski[15], B.A. Popov[19,4], B. Porfy[7], M. Posiadała-Zezula[15], D.S. Prokhorova[21], D. Pszczel[11], S. Puławski[14], J. Puzović[22], M. Ravonel[23], R. Renfordt[6], D. Röhrich[8], E. Rondio[11], M. Roth[5], B.T. Rumberger[25], M. Rumyantsev[19], A. Rustamov[1,6], M. Rybczynski[9], A. Rybicki[10], S. Sadhu[9], A. Sadovsky[18], K. Schmidt[14], I. Selyuzhenkov[20], A.Yu. Seryakov[21], P. Seyboth[9], M. Słodkowski[17], P. Staszel[12], G. Stefanek[9], J. Stepaniak[11], M. Strikhanov[20], H. Ströbele[6], T. Šuša[3], A. Taranenko[20], A. Tefelska[17], D. Tefelski[17], V. Tereshchenko[19], A. Toia[6], R. Tsenov[2], L. Turko[16], R. Ulrich[5], M. Unger[5], D. Uzhva[21], F.F. Valiev[21], D. Veberič[5], V.V. Vechernin[21], A. Wickremasinghe[26,24], Z. Włodarczyk[9], K. Wojcik[14], O. Wyszyński[9], E.D. Zimmerman[25], and R. Zwaska[24]

[1] National Nuclear Research Center, Baku, Azerbaijan
[2] Faculty of Physics, University of Sofia, Sofia, Bulgaria
[3] Ruđer Bošković Institute, Zagreb, Croatia
[4] LPNHE, University of Paris VI and VII, Paris, France
[5] Karlsruhe Institute of Technology, Karlsruhe, Germany
[6] University of Frankfurt, Frankfurt, Germany
[7] Wigner Research Centre for Physics of the Hungarian Academy of Sciences, Budapest, Hungary
[8] University of Bergen, Bergen, Norway
[9] Jan Kochanowski University in Kielce, Poland
[10] Institute of Nuclear Physics, Polish Academy of Sciences, Cracow, Poland
[11] National Centre for Nuclear Research, Warsaw, Poland
[12] Jagiellonian University, Cracow, Poland
[13] AGH - University of Science and Technology, Cracow, Poland
[14] University of Silesia, Katowice, Poland
[15] University of Warsaw, Warsaw, Poland
[16] University of Wrocław, Wrocław, Poland
[17] Warsaw University of Technology, Warsaw, Poland
[18] Institute for Nuclear Research, Moscow, Russia
[19] Joint Institute for Nuclear Research, Dubna, Russia
[20] National Research Nuclear University (Moscow Engineering Physics Institute), Moscow, Russia
[21] St. Petersburg State University, St. Petersburg, Russia
[22] University of Belgrade, Belgrade, Serbia
[23] University of Geneva, Geneva, Switzerland

[24] Fermilab, Batavia, USA
[25] University of Colorado, Boulder, USA
[26] University of Pittsburgh, Pittsburgh, USA

1 Introduction

This paper presents experimental results on inclusive spectra and mean multiplicities of $\pi^{\pm}, K^{\pm}, p$ and $\bar{p}$ produced in the 20% most *central* ^{7}Be+^{9}Be collisions at beam momenta of 19A, 30A, 40A, 75A and 150A GeV/c ($\sqrt{s_{NN}}$= 6.1, 7.6, 8.8, 11.9 and 16.8 GeV). These studies form part of the strong interactions programme of NA61/SHINE [1] investigating the properties of the onset of deconfinement and searching for the possible existence of a critical point. This requires a two dimensional scan in collision energy and nuclear mass number of the colliding nuclei. Such a scan allows to explore systematically the phase diagram of strongly interacting matter [1]. An increase of collision energy causes an increase of temperature and a decrease of baryon chemical potential of strongly interacting matter at freeze-out, whereas increasing the nuclear mass number of the colliding nuclei decreases the temperature [2].

Pursuing this programme NA61/SHINE recorded data on p+p, Be+Be, Ar+Sc, Xe+La and Pb+Pb collisions. Moreover, further measurements of Pb+Pb interactions are planned with an upgraded detector [3] starting in 2021.

The ^{7}Be+^{9}Be collisions (see Ref. [4] for results on π^{-} production) play a special role in the NA61/SHINE scan programme. First, it was predicted within the statistical models [5,6] that the yield ratio of strange hadrons to pions in these collisions should be close to those in central Pb+Pb collisions and significantly higher than in p+p interactions. Second, the collision system composed of a ^{7}Be and a ^{9}Be nucleus has eight protons and eight neutrons, and thus is isospin symmetric. Within the NA61/SHINE scan programme the ^{7}Be+^{9}Be collisions serve as the lowest mass isospin symmetric reference needed to study collisions of medium and large mass nuclei. This is of particular importance when data on proton-proton, neutron-proton and neutron-neutron are not available to construct the nucleon-nucleon reference [7].

The paper is organized as follows: after this introduction the experiment is briefly presented in Sec. 2. The analysis procedure, as well as statistical and systematic uncertainties are discussed in Sec. 3. Section 4 presents experimental results and compares them with measurements of NA61/SHINE in inelastic p+p interactions [8–10] and NA49 in Pb+Pb collisions [11, 12]. Section 5 discusses model predictions. A summary in Sec. 6 closes the paper.

The following variables and definitions are used in this paper. The particle rapidity y is calculated in the collision center of mass system (cms), $y = 0.5 \cdot ln[(E + p_L)/(E - p_L)]$, where E and p_L are the particle energy and longitudinal momentum, respectively. The transverse component of the momentum is denoted as p_T and the transverse mass m_T is defined as $m_T = \sqrt{m^2 + (cp_T)^2}$ where m is the particle mass in GeV. The momentum in the laboratory frame is denoted p_{lab} and the collision energy per nucleon pair in the center of mass by $\sqrt{s_{NN}}$.

Results of the measurements correspond to collisions with low energy emitted into the forward beam spectator region. For ^{7}Be+^{9}Be collisions this energy is not tightly correlated with geometric parameters of the interaction such as the collision impact parameter of the collision (see Sec. 3.1). This is caused by the small number of nucleons and the cluster structure of the Be nucleus. Nevertheless, following the

convention widely used in the analysis of nucleus-nucleus collisions, the term *central* is used for events selected by imposing an upper limit on this energy.

2 Experimental setup of NA61/SHINE

2.1 Detector

The NA61/SHINE experiment is a multi-purpose facility designed to measure particle production in nucleus+nucleus, hadron+nucleus and $p+p$ interactions [13]. The detector is situated at the CERN Super Proton Synchrotron (SPS) in the H2 beamline of the North experimental area. A schematic diagram of the setup is shown in Fig. 1. The main components of the produced particle detection system are four
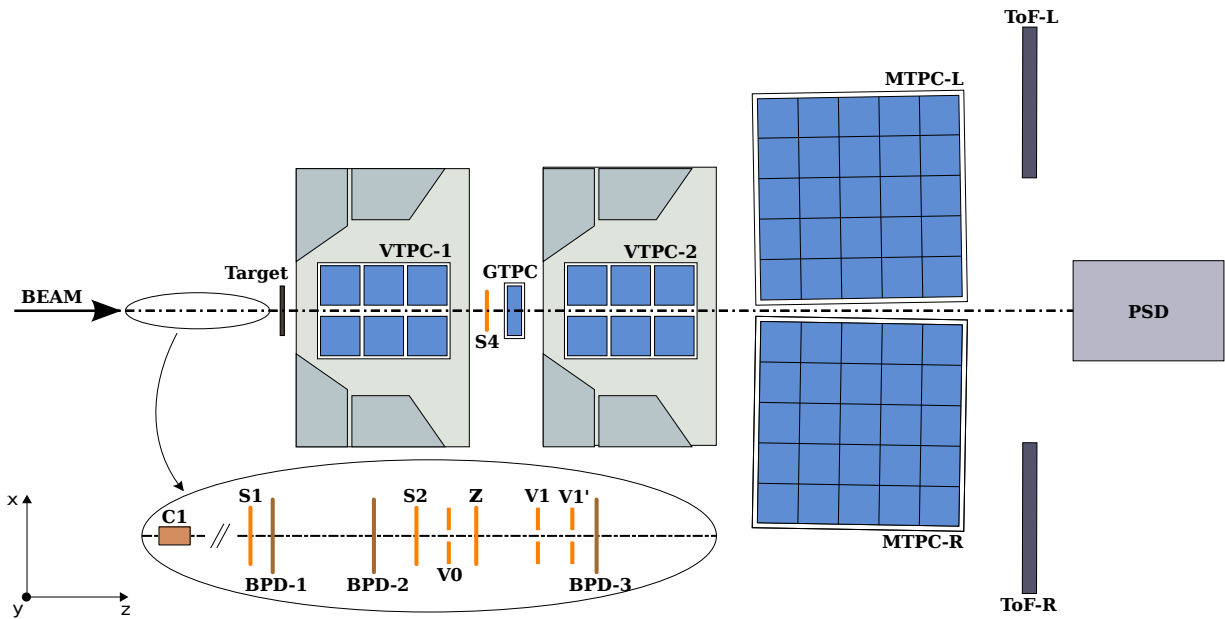

Figure 1: The schematic layout of the NA61/SHINE experiment at the CERN SPS [13] showing the components used for the Be+Be energy scan (horizontal cut, not to scale). The beam instrumentation is sketched in the inset (see also Fig. 2). Alignment of the chosen coordinate system as shown in the figure: its origin lies in the middle of VTPC-2, on the beam axis. The nominal beam direction is along the z-axis. The magnetic field bends charged particle trajectories in the x–z (horizontal) plane. The drift direction in the TPCs is along the y (vertical) axis.

large volume Time Projection Chambers (TPC). Two of them, called Vertex TPCs (VTPC), are located downstream of the target inside superconducting magnets with maximum combined bending power of 9 Tm. The magnetic field was scaled down in proportion to the beam momentum in order to obtain similar phase space acceptance at all energies. The main TPCs (MTPC) and two walls of pixel Time-of-Flight (ToF-L/R) detectors are placed symmetrically to the beamline downstream of the magnets. The fifth small TPC (GAP-TPC) is placed between VTPC1 and VTPC2 directly on the beam line. The TPCs are filled with Ar:CO_2 gas mixtures in proportions 90:10 for the VTPCs and the GAP-TPC, and 95:5 for the MTPCs.

The Projectile Spectator Detector (PSD), which measures mainly the energy in the forward region of projectile spectators, is positioned 20.5 m (16.7 m) downstream of the target during measurements at $75A$ and $150A$ GeV/c ($19A$, $30A$, $40A$ GeV/c) centered in the transverse plane on the position of the deflected

beam. The PSD is used as a part of the trigger system (see Sec.2.2) to accept collisions by imposing an upper limit on the energy measured in the 16 central modules and also to select *central* events in analysis procedure (see Sec.3.1).

The beamline instrumentation is schematically depicted in Fig. 2. It is designed for obtaining high beam purity with secondary ion beams [14] produced by fragmenting the primary Pb^{82+} ions extracted from the SPS. A detailed discussion of the properties of selected ^7Be ions can be found in Ref. [4].

A set of scintillation counters as well as beam position detectors (BPDs) upstream of the spectrometer provide timing reference, selection, identification and precise measurement of the position and direction of individual beam particles.
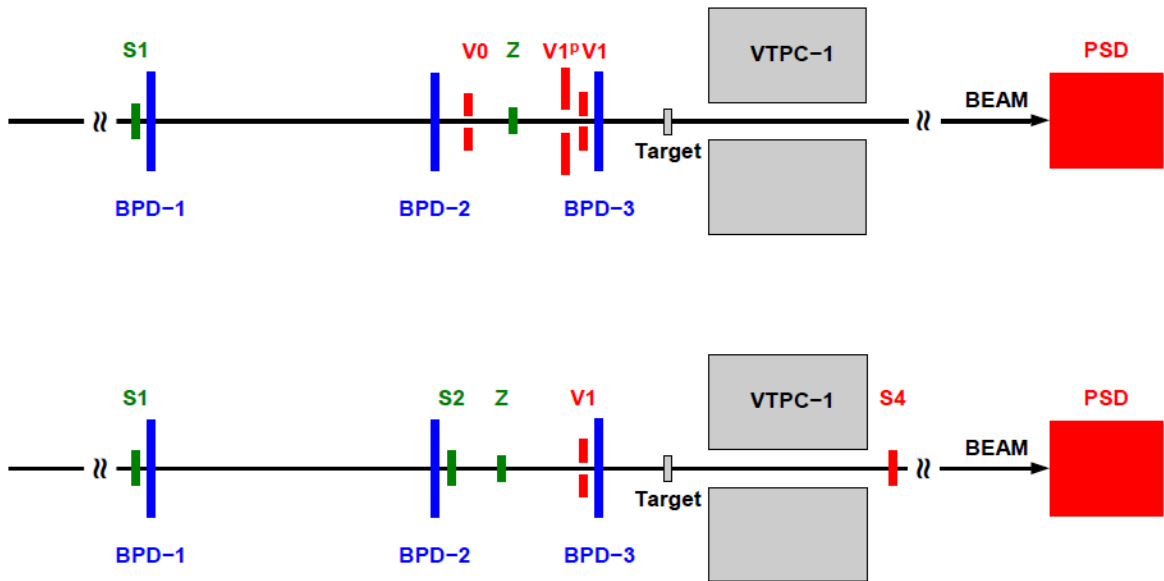

Figure 2: The schematic of the placement of the beam and trigger detectors in high-momentum *(top)* and low-momentum *(bottom)* data taking configurations showing beam counters S, veto counters V and beam position and charge detectors BPD, as well as a Cerenkov detector Z. Note, that the PSD calorimeter was almost 4 m closer for low momentum data taking.

The target was a plate of ^9Be of 12 mm thickness placed ≈ 80 cm upstream of VTPC1. Mass concentrations of impurities in the target were measured at 0.3%, resulting in an estimated increase of the produced pion multiplicity by less than 0.5% due to the small admixture of heavier elements [15]. No correction was applied for this negligible contamination. Data were taken with target inserted (denoted I, 90%) and target removed (denoted R, 10%).

2.2 Trigger

The schematic of the placement of the beam and trigger detectors can be seen in Fig. 2. The trigger detectors consist of a set of scintillation counters recording the presence of the beam particle (S1, S2), a set of veto scintillation counters with a hole used to reject beam particles passing far from the centre

Table 1: Basic beam properties and number of events recorded and used in the analysis for Be+Be interactions of the 20% most *central* collisions.

p_{beam} [$AGeV/c$]	$\sqrt{s_{NN}}$ [GeV]	Number of event triggers	Number of events after selection cuts
19	6.1	$3.46 \cdot 10^6$	$1.32 \cdot 10^5$
30	7.6	$5.41 \cdot 10^6$	$1.48 \cdot 10^5$
40	8.8	$3.42 \cdot 10^6$	$3.97 \cdot 10^5$
75	11.9	$5.24 \cdot 10^6$	$3.99 \cdot 10^5$
150	16.8	$2.93 \cdot 10^6$	$3.25 \cdot 10^5$

of the beamline (V0, V1), and a Cherenkov charge detector (Z). Beam particles were defined by the coincidence T1 = S1·S2·$\overline{\text{V1}}$·Z(Be) and T1 = S1·$\overline{\text{V0}}$·$\overline{\text{V1}}$·$\overline{\text{V1'}}$·Z(Be) for low and high momentum data taking respectively. An interaction trigger detector (S4) was used to check whether the beam particle changed charge after passing through the target. In addition, collisions were selected by requiring an energy signal below a set threshold from the 16 central modules of the PSD. The event trigger condition thus was T2 = T1·$\overline{\text{S4}}$·$\overline{\text{PSD}}$ or T2 = T1·$\overline{\text{PSD}}$ for low and high beam momenta, respectively. The PSD threshold was set to retain from $\approx 70\%$ to $\approx 40\%$ of inelastic collisions at low and high beam momenta, respectively. The statistics of recorded events is summarised in Table 1.

3 Analysis procedure

This section starts with a brief overview of the data analysis procedure and the applied corrections. It also defines to which class of particles the final results correspond. A description of the calibration and the track and vertex reconstruction procedures can be found in Ref. [8].

The analysis procedure consists of the following steps:

(i) application of event and track selection criteria,

(ii) determination of raw spectra of identified charged hadrons using the selected events and tracks,

(iii) evaluation of corrections to the raw spectra based on experimental data and simulations,

(iv) calculation of the corrected spectra and mean multiplicities,

(v) calculation of statistical and systematic uncertainties.

Corrections for the following biases were evaluated:

(a) contribution from off-target interactions,

(b) losses of in-target interactions due to the event selection criteria,

(c) geometrical acceptance,

(d) reconstruction and detector inefficiency,

(e) losses of tracks due to track selection criteria,

(f) contribution of particles other than *primary* (see below) charged particles produced in Be+Be interactions,

(g) losses of primary charged particles due to their decays and secondary interactions.

Correction (a) was not applied due to insufficient statistics of the target removed data. The contamination of the target inserted data was estimated from the z distribution of fitted vertices to amount to $\approx 0.35\%$.

Corrections (b)-(g) were estimated by data and simulations. MC events were generated with the EPOS1.99 model (version CRMC 1.5.3) [16], passed through detector simulation employing the GEANT 3.21 package [17] and then reconstructed by the standard program chain.

The final results refer to particles produced in *central* Be+Be collisions by strong interaction processes and in electromagnetic decays of produced hadrons. Such hadrons are referred to as *primary* hadrons. *Central* collisions refer to events selected by a cut on the total energy emitted into the forward direction as defined by the acceptance maps for the PSD given in Ref. [18].

The analysis was performed in (y, p_T) bins. The bin size was chosen taking into account the statistical uncertainties and the resolution of the momentum reconstruction [8]. Corrections as well as statistical and systematic uncertainties were calculated for each bin.

3.1 *Central* collisions

A short description of the procedure for defining *central* collisions is given below. For more details see Refs. [4, 19].

Final results presented in this paper refer to Be+Be collisions with the 20% lowest values of the forward energy E_F (*central* collisions). The quantity E_F is defined as the total energy in the laboratory system of all particles produced in a Be+Be collision via strong and electromagnetic processes in the forward momentum region defined by the acceptance map in Ref. [18]. Final results on *central* collisions, derived using this procedure, allow a precise comparison with predictions of models without any additional information about the NA61/SHINE setup and used magnetic field.

For analysis of the data the event selection was based on the $\approx 20\%$ of collisions with the lowest value of the energy E_{PSD} measured by a subset of PSD modules (see Fig. 3) in order to optimize the sensitivity to projectile spectators. The forward momentum acceptance in the definition of E_F corresponds closely to the acceptance of this subset of PSD modules.

Online event selection by the hardware trigger (T2) used a threshold on the electronic sum of energies over the 16 central modules of the PSD set to accept $\approx 40\%$ of the inelastic interactions. The minimum-bias distribution was obtained using the data from the beam trigger T1 with offline selection of events by requiring an event vertex in the target region and a cut on the ionisation energy detected in the GTPC to exclude Be beams. The spectrum of E_{PSD} was calculated for the subset of modules and a properly normalized spectrum for target removed events was subtracted. Events for further analysis were selected by applying a cut in this distribution for the 20% of events with the smallest values of E_{PSD}. More details on the PSD modules selection optimisation and E_{PSD} determination can be found in [19].

The forward energy E_F cannot be measured directly. However, both E_F and E_{PSD} can be obtained from simulations using the EPOS1.99 (version CRMC 1.5.3) [16] model. A global factor c_{cent} (listed in
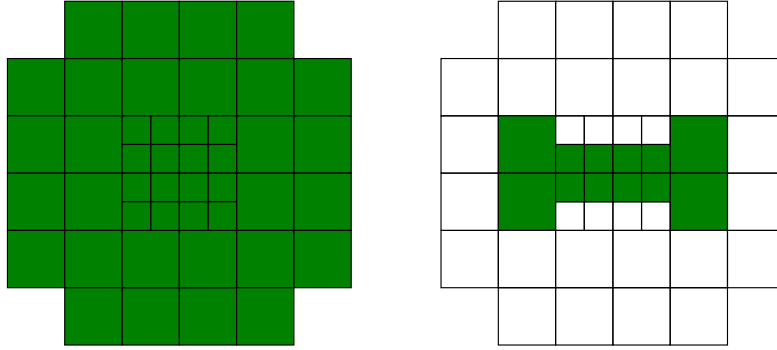
Figure 3: PSD modules included in the calculation of the projectile spectator energy E_{PSD} used for event selection for beam momenta of 19A, and 30A GeV/c (*left*) and for 40A, 75A and 150A GeV/c (*right*)

Table 2) was then calculated as the ratio of mean negatively charged pion multiplicities obtained with the two selection procedures for 20% of all inelastic collisions. A possible dependence of the scaling factor on rapidity and transverse momentum was neglected. The resulting factors c_{cent} range from 1.00 and 1.04 which is only a small correction compared to the systematic uncertainties of the measured particle multiplicities. The correction was therefore not applied, but instead included in the systematic uncertainty.

Finally, the average number of wounded nucleons $\langle W \rangle$ and the average collision impact parameter $\langle b \rangle$ were calculated within the Wounded Nucleon Model [20] implemented in EPOS for events with the 20% smallest values of E_F. Results are listed in Table 2. Example distributions for the top beam momentum are shown in Fig. 4. As the Be nucleus consists of few nucleons these distributions are quite broad. For comparison $\langle W \rangle$ and $\langle b \rangle$ were also calculated from the GLISSANDO model [21] which uses a different Glauber model calculation. The results, also listed in Table 2, differ by about 10% for $\langle W \rangle$. This discrepancy was included in the systematic error estimate (see Sec. 3.5.2) .

3.2 Event and track selection

3.2.1 Event selection

For further analysis Be+Be events were selected using the following criteria:

(i) four units of charge measured in S1, S2, and Z counters as well as BPD3 (this requirement also rejects most interactions upstream of the Be target),

(ii) no off-time beam particle detected within a time window of $\pm 4.5\,\mu$s around the trigger particle,

(iii) no other event trigger detected within a time window of $\pm 25\,\mu$s around the trigger particle,
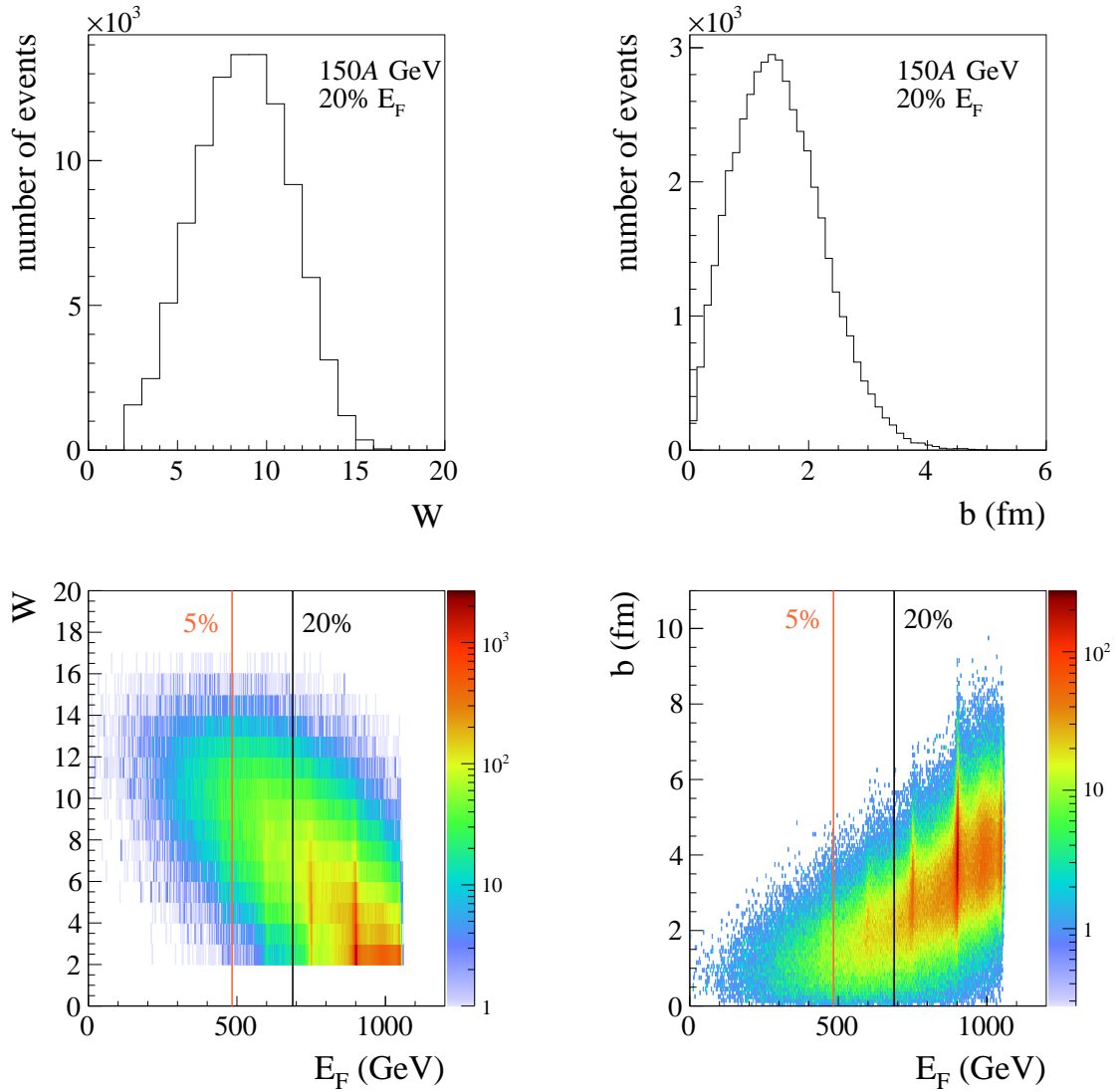
8

Figure 4: Examples of the distribution of the number of wounded nucleons W (*left*) and collision impact parameter b (*right*) for events with the 20% smallest forward energies E_F *(central)* at beam momentum of 150A GeV/c simulated with the EPOS model using the acceptance map provided in Ref. [18].

(iv) beam particle detected in at least two planes out of four of BPD-1 and BPD-2 and in both planes of BPD-3,

(v) a well reconstructed interaction vertex with z position (fitted using the beam trajectory and TPC tracks) not farther away than 15 cm from the center of the Be target (the cut removes less than 0.4% of T2 trigger (E_{PSD}) selected interactions),

(vi) an upper cut on the measured energy E_{PSD} which selects 20% of all inelastic collisions.

The event statistics after applying the selection criteria is summarized in Table 1.

Table 2: Average number of wounded nucleons $\langle W \rangle$ and average collision impact parameter $\langle b \rangle$ in the 20% most *central* Be+Be collisions estimated from simulations using the EPOS [16] and GLISSANDO [21] models. The values of σ denote the widths of the distributions of W and b. Results EPOS WNM and Glissando are for *centrality* selection using the smallest number of spectators in the Glauber model. EPOS E_F results correspond to selecting events by the forward energy E_F within the acceptance map in Ref. [18]. Also shown are correction factors c_{cent} needed to account for the different event selection procedures used for the data (measured E_{PSD}) and the simulation (simulated values of E_F).

Momentum (A GeV/c)		19	30	40	75	150
EPOS E_F *(central)*	$\langle W \rangle$	8.04	7.99	8.13	8.12	8.15
	σ	2.6	2.6	2.6	2.6	2.6
	$\langle b \rangle$	1.89	1.93	1.49	1.49	1.51
	σ	0.9	0.9	0.7	0.7	0.7
EPOS Glauber	$\langle W \rangle$	8.87	8.88	8.89	8.90	8.93
	σ	1.8	1.8	1.8	1.8	1.8
GLISSANDO	$\langle W \rangle$	8.74	8.77	8.76	8.83	8.91
	σ	1.78	1.79	1.80	1.80	1.81
	c_{cent}	1.003	1.043	1.008	1.016	1.027

3.2.2 Track selection

In order to select tracks of primary charged hadrons and to reduce the contamination by particles from secondary interactions, weak decays and off-time interactions, the following track selection criteria were applied:

(i) track momentum fit including the interaction vertex should have converged,

(ii) fitted $\times$ component of particle rigidity $q \cdot p_{lab}$ is positive. This selection minimizes the angle between the track trajectory and the TPC pad direction for the chosen magnetic field direction, reducing uncertainties of the reconstructed cluster position, energy deposition and track parameters,

(iii) total number of reconstructed points on the track should be greater than 30,

(iv) sum of the number of reconstructed points in VTPC-1 and VTPC-2 should be greater than 15 or greater than 4 in the GTPC,

(v) the distance between the track extrapolated to the interaction plane and the (track impact parameter) should be smaller than 4 cm in the horizontal (bending) plane and 2 cm in the vertical (drift) plane.

3.3 Identification techniques

Charged particle identification in the NA61/SHINE experiment is based on the ionization energy loss, dE/dx, in the gas of the TPCs and the time of flight, tof, obtained from the ToF-L and ToF-R walls. In the region of the relativistic rise of the ionization at large momenta the measurement of dE/dx alone allows identification. At lower momenta the dE/dx bands for different particle species overlap and additional measurement of tof is required to remove the ambiguity. These two methods allow to cover most of the phase space in rapidity and transverse momentum which is of interest for the strong interaction programme of NA61/SHINE. The acceptance of the two methods is shown in Figs. 5 and 6 for the 20% most *central* Be+Be interactions at 30 and 150A GeV/c, respectively. At low beam energies the tof-dE/dx method

extends the identification acceptance, while at top SPS energy it overlaps with the dE/dx method (for more details see Ref. [22]).
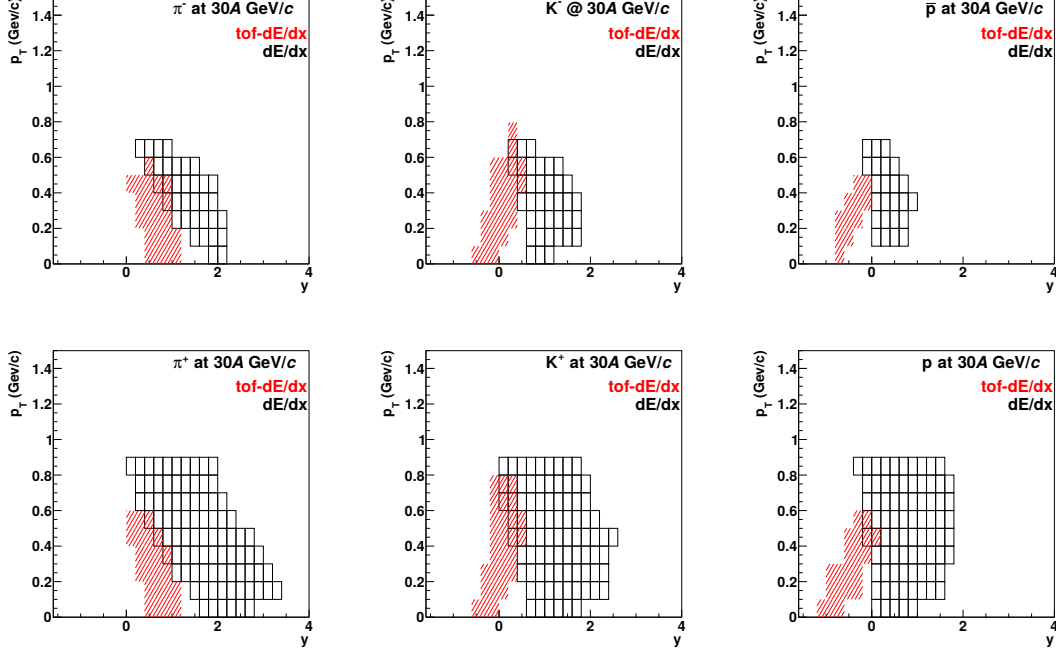

Figure 5: Acceptance of the tof-dE/dx and dE/dx methods for identification of pions, kaons and protons in the 20% most *central* Be+Be interactions at 30A GeV/c.

3.3.1 Identification based on energy loss measurement (dE/dx)

Time projection chambers provide measurements of energy loss dE/dx of charged particles in the chamber gas along their trajectories. Simultaneous measurements of dE/dx and p_{lab} allow to extract information on particle mass. The mass assignment follows the procedure which was developed for the analysis of $p+p$ reactions as described in Ref. [9]. Values of dE/dx are calculated as the truncated mean (smallest 50%) of ionisation energy loss measurements along the track trajectory. As an example, dE/dx measured in the 20% most central Be+Be interactions at 75A GeV/c is presented in Fig. 7, for positively and negatively charged particles, as a function of $q \cdot p_{\text{lab}}$.

The contributions of e^+, e^-, π^+, π^-, K^+, K^-, p and $\bar{p}$ are obtained by fitting the dE/dx distributions separately for positively and negatively charged particles in bins of p_{lab} and p_T with a sum of four functions [23, 24] each corresponding to the expected dE/dx distribution for the corresponding particle type. The small contribution of light (anti-)nuclei was neglected.

In order to ensure similar particle multiplicities in each bin, 20 logarithmic bins are chosen in p_{lab} in the range $1 - 100$ GeV/c to cover the full detector acceptance. Furthermore, the data are binned in 20 equal p_T intervals in the range 0-2 GeV/c.

The distribution of dE/dx for tracks of a given particle type i is parameterised as the sum of Gaussians with widths $\sigma_{i,l}$ depending on the particle type i and the number of points l measured in the TPCs. Simplifying
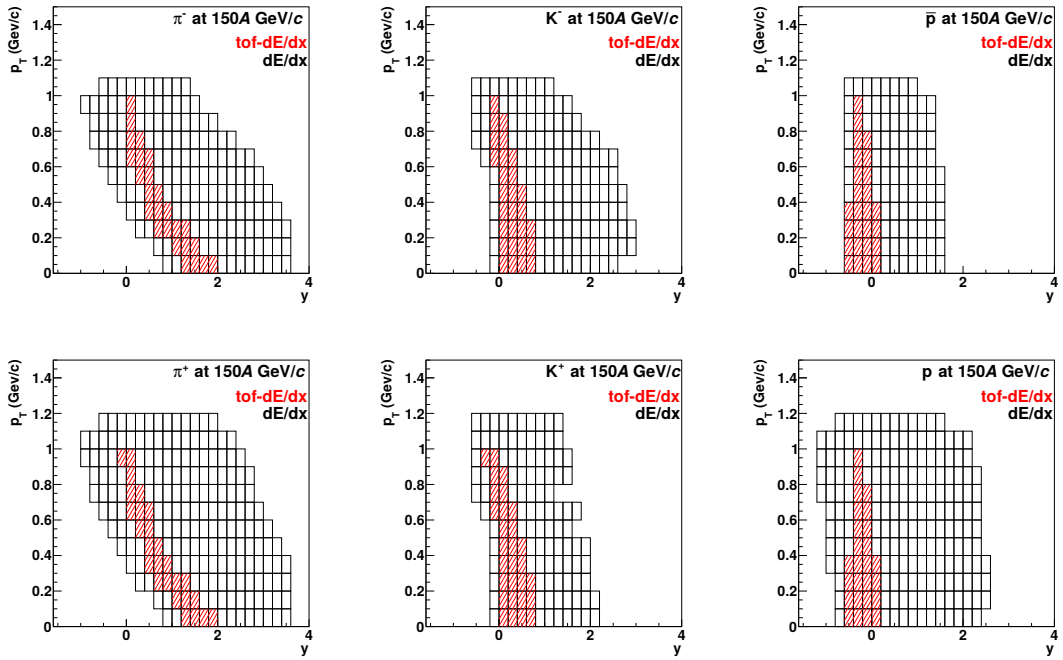
Figure 6: Acceptance of the tof-dE/dx and dE/dx methods for identification of pions, kaons and protons in the 20% most *central* Be+Be interactions at 150A GeV/c.
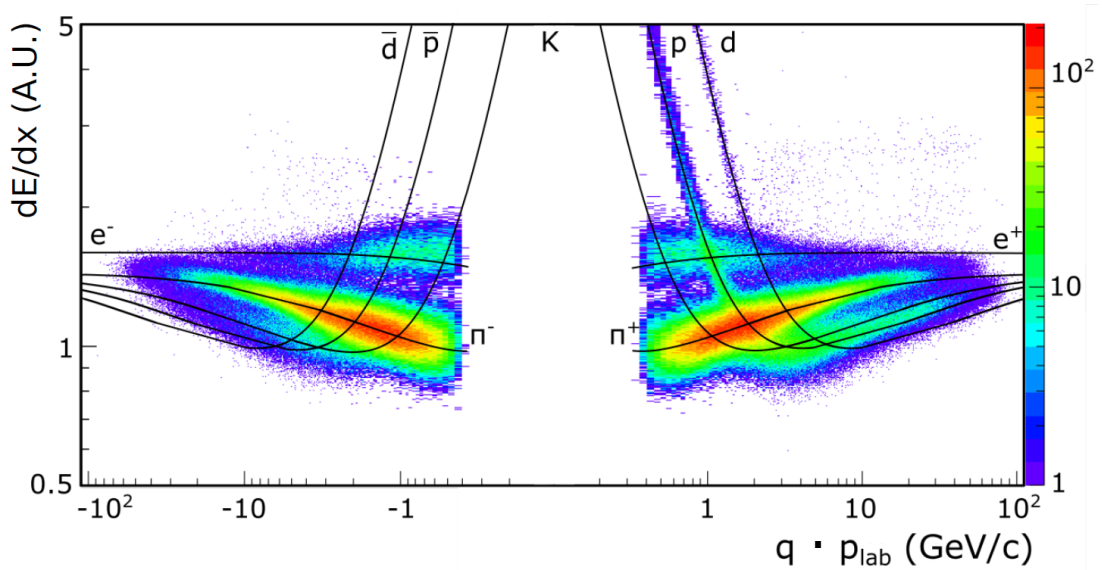

Figure 7: Distribution of charged particles in the $dE/dx - q \cdot p_{lab}$ plane. The energy loss in the TPCs for different charged particles for events and tracks selected for the analysis of Be+Be collisions at 75A GeV/c (the target inserted configuration). Expectations for the dependence of the mean dE/dx on p_{lab} for the considered particle types are shown by the curves calculated based on the Bethe-Bloch function.

the notation in the fit formulae, the peak position of the dE/dx distribution for particle type i is denoted as x_i. The contribution of a reconstructed particle track to the fit function reads:

$$\rho(x) = \sum_i \rho_i(x) = \sum_{i=\pi,p,K,e} A_i \frac{1}{\sum_l n_l} \sum_l \frac{n_l}{\sqrt{2\pi}\sigma_l} exp\left[-\frac{1}{2}\left(\frac{x-x_i}{\sigma_l}\right)^2\right], \tag{1}$$

where x is the dE/dx of the particle, n_l is the number of tracks with number of points l in the sample and A_i is the amplitude of the contribution of particles of type i. The second sum is the weighted average of the line-shapes from the different numbers of measured points (proportional to track-length) in the sample. The quantity σ_l is written as:

$$\sigma_l = \sigma_0 \left(\frac{x_i}{x_\pi}\right)^{0.625} / \sqrt{n_l}, \tag{2}$$

where the width parameter σ_0 is assumed to be common for all particle types and bins. A $1/\sqrt{l}$ dependence on number of points is assumed. The Gaussian peaks could in principle be asymmetric if the tail of the Landau distribution persists to some extent even after truncation (for detail see [25]). However, no significant effect was found.

The fit function has 9 parameters (4 amplitudes, 4 peak positions and width) which are difficult to fit in each bin independently. Therefore the following constraints on the fitting parameters were adopted:

  (i) positions of electrons, kaons and protons relative to pions were assumed to be p_T-independent,

  (ii) the fitted amplitudes were required to be greater than or equal to 0,

  (iii) the electron amplitude was set to zero for total momentum p_{lab} above 23.4 GeV/c (i.e. starting from the 13th bin), as the electron contribution vanishes at high p_{lab},

  (iv) if possible, the relative position of the positively charged kaon peak was taken to be the same as that of negatively charged kaons determined from the negatively charged particles in the bin of the same p_{lab} and p_T. This procedure helps to overcome the problem of the large overlap between K^+ and protons in the dE/dx distributions.

The constraints reduce the number of independently fitted parameters in each bin from 9 to 6, i.e. the amplitudes of the four particle types, the pion peak position and the width parameter σ_0.

Examples of fits are shown in Fig. 8 and the values of the fitted peak positions x_i are plotted in Fig. 9 versus momentum for different particle types i in selected Be+Be interactions at 150 A GeV/c. As expected, the values of x_i increase with p_{lab} but do not depend on p_T.

In order to ensure good fit quality, only bins with total number of tracks grater than 1000 (500 in the 19A GeV/c sample) are used for further analysis. The Bethe-Bloch curves for different particle types cross each other at low values of the total momentum. Thus, the technique is not sufficient for particle identification at low p_{lab} and bins with $p_{lab} < 3.98$ GeV/c (bins 1-5) are excluded from the analysis based solely on dE/dx measurements.
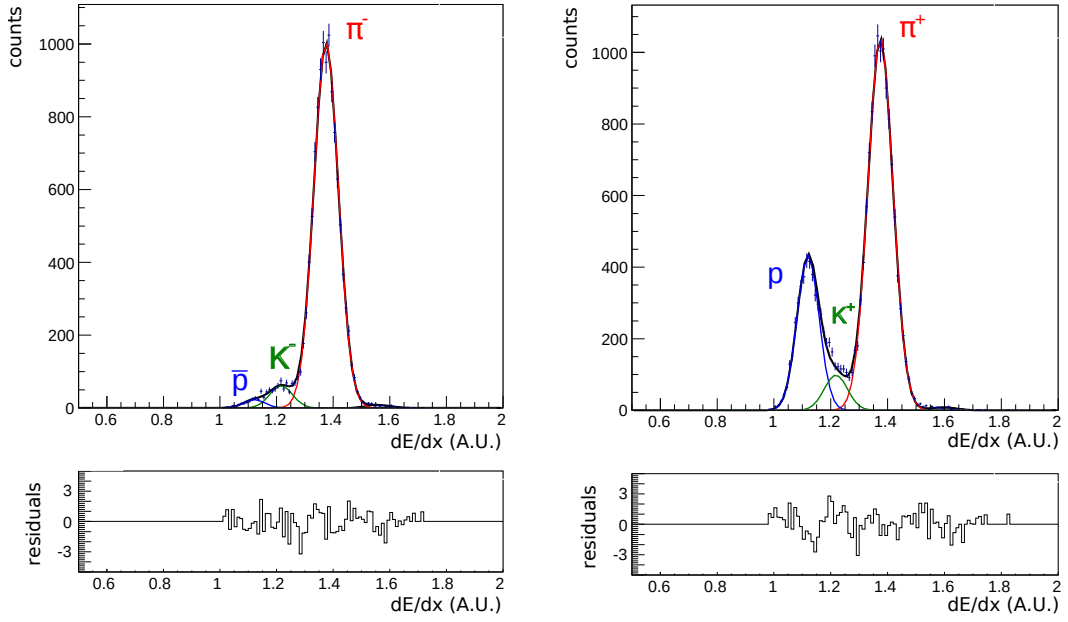
Figure 8: The dE/dx distributions for negatively (*top, left*) and positively (*top, right*) charged particles in the bin $12.6 \le p_{\text{lab}} \le 15.8$ GeV/c and $0.2 \le p_T \le 0.3$ GeV/c produced in PSD selected Be+Be collisions at $75A$ GeV/c. The fit by a sum of contributions from different particle types is shown by solid lines. The corresponding residuals (the difference between the data and fit divided by the statistical uncertainty of the data) is shown in the bottom plots.
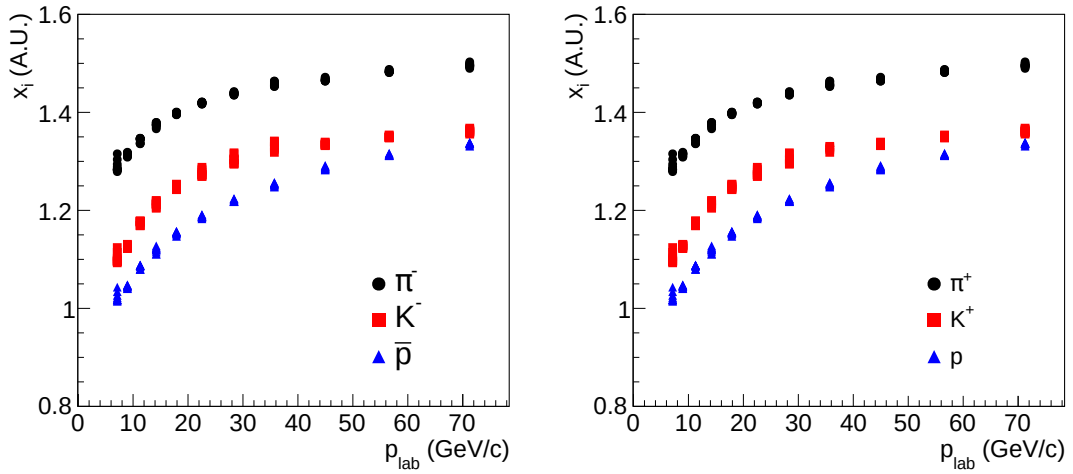

Figure 9: Fitted peak positions in selected Be+Be interactions at $150\,A$ GeV/c for different particles as a function of p_{lab}. The x_i for different p_T at each p_{lab} show little variation and mostly overlap.

14

3.3.2 Identification based on time of flight and energy loss measurements (tof-dE/dx)

Identification of π^+, π^-, K^+, K^-, p and $\bar{p}$ at low momenta (from 2-8 GeV/c) is possible when measurement of dE/dx is combined with time of flight information tof. Timing signals from the constant-fraction discriminators and signal amplitude information are recorded for each tile of the ToF-L/R walls. Only hits which satisfy quality criteria (see Ref. [26] for detail) are selected for the analysis. The coordinates of the track intersection with the front face are used to match the track to tiles with valid tof hits. The position of the extrapolation point on the scintillator tile is used to correct the measured value of tof for the propagation time of the light signal. The distribution of the difference between the corrected tof measurement and the value calculated from the extrapolated track trajectory length with the assumed mass hypothesis can be well described by a Gaussian with standard deviation of 80 ps for ToF-R and 100 ps for ToF-L. These values represent the tof resolution including all detector effects.

Momentum phase space is subdivided into bins of 1 GeV/c in p_{lab} and 0.1 GeV/c in p_T. Only bins with more than 200 (500 in the 150A GeV/c sample) entries were used for extracting yields with the tof-dE/dx method.
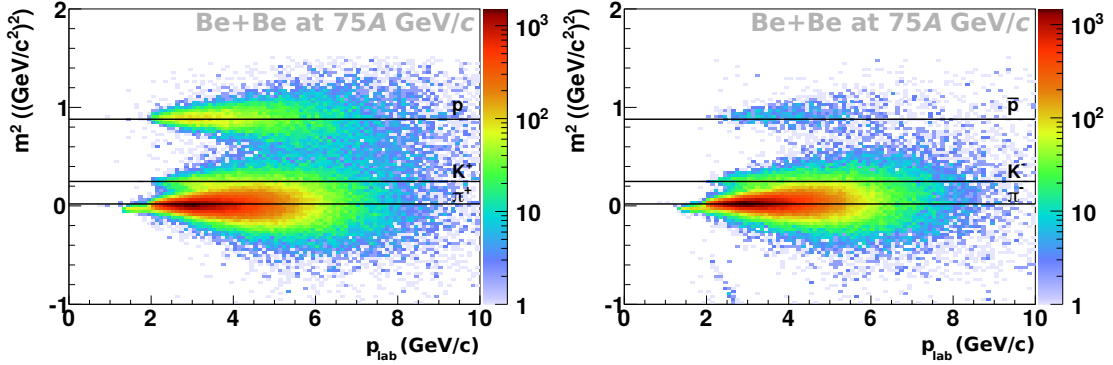

Figure 10: Mass squared derived using time-of-flight measured by ToF-R (*right*) and ToF-L (*left*) versus laboratory momentum for particles produced in PSD selected Be+Be collisions at 75A GeV/c (target inserted configuration). The lines show the expected mass squared values for different hadrons species.

The square of the particle mass m^2 is obtained from tof, the momentum p and the fitted trajectory length l:

$$m^2 = (cp)^2 \left(\frac{c^2\, tof^2}{l^2} - 1 \right) . \tag{3}$$

For illustration distributions of m^2 versus p_{lab} are plotted in Fig. 10 for positively (*left*) and negatively (*right*) charged hadrons produced in Be+Be interactions at 75A GeV/c. Bands which correspond to different particle types are visible. Separation between pions and kaons is possible up to momenta of about 5 GeV/c, between pions and protons up to about 8 GeV/c.

Example distributions of particles in the m^2–dE/dx plane for the selected Be+Be interactions at 40A GeV/c are presented in Fig. 11. Simultaneous dE/dx and tof measurements lead to improved separation between different hadron types. In this case a simple Gaussian parametrization of the dE/dx distribution for a given hadron type can be used.
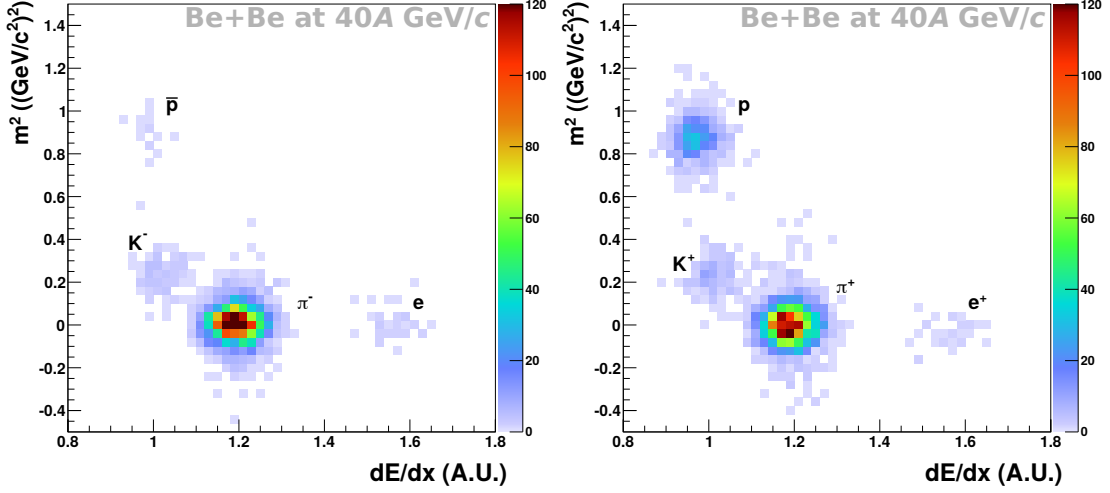
Figure 11: Particle number distribution in the m^2-dE/dx plane for negatively (*left*) and positively (*right*) charged particles with momenta $3 < p_{lab} < 4$ GeV/c and $0.3 < p_T < 0.4$ GeV/c) for PSD selected Be+Be collisions at $40A$ GeV/c.

The tof-dE/dx identification method proceeds by fitting the 2-dimensional distribution of particles in the dE/dx -m^2 plane. Fits were performed in the momentum range from 1-8 GeV/c and transverse momentum range 0-1 GeV/c. For positively charged particles the fit function included contributions of p, K^+, π^+ and e^+, and for negatively charged particles the corresponding anti-particles were considered. The fit function for a given particle type was assumed to be a product of a Gauss function in dE/dx and a sum of two Gauss functions in m^2 (in order to describe the broadening of the m^2 distributions with momentum). In order to simplify the notation in the fit formulae, the peak positions of the dE/dx and m^2 Gaussians for particle type j are denoted as x_j and y_j, respectively. The contribution of a reconstructed particle track to the fit function reads:

$$
\begin{aligned}
\rho(x,y) &= \sum_{j=p,\pi,K,e} \rho_j(x,y) \\
&= \sum_j \frac{N_j}{2\pi\,\sigma_x} exp\left[-\frac{(x-x_j)^2}{2\sigma_x^2}\right] \left(\frac{f}{\sigma_{y_1}} exp\left[\frac{(y-y_j)^2}{2\sigma_{y_1}^2}\right] + \frac{(1-f)}{\sigma_{y_2}} exp\left[\frac{(y-y_j)^2}{2\sigma_{y_2}^2}\right]\right),
\end{aligned}
\tag{4}
$$

where N_j and f are amplitude parameters, x_j, σ_x are means and width of the dE/dx Gaussians and y_j, σ_{y1}, σ_{y2} are mean and width of the m^2 Gaussians, respectively. The total number of parameters in Eq. 4 is 16. Imposing the constraint of normalisation to the total number of tracks N in the kinematic bin

$$
N = \sum_i N_i
\tag{5}
$$

the number of parameters is reduced to 15. Two additional assumptions were adopted:

  (i) the fitted amplitudes were required to be greater than or equal to 0,

 (ii) $\sigma_{y1} < \sigma_{y2}$ and $f > 0.7$, the "core" distribution dominates the m^2 fit.

16

An example of the tof-dE/dx fit obtained in a single phase-space bin for positively charged particles in PSD selected Be+Be collisions at $40A$ GeV/c is shown in Fig. 12.
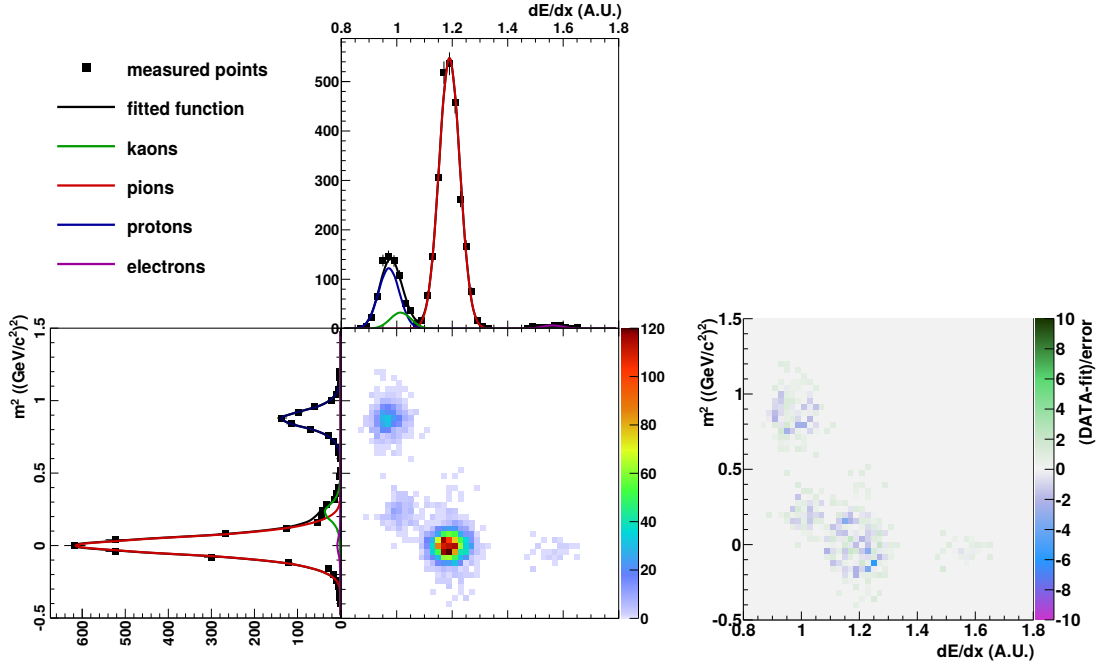

Figure 12: Example of the tof-dE/dx fit (Eq. 4) obtained in a single phase-space bin ($3 < p_{\text{lab}} < 4$ GeV/c and $0.3 < p_T < 0.4$ GeV/c) for positively charged particles in PSD selected Be+Be collisions at $40A$ GeV/c. Lines show projections of the fits for pions (red), kaons (green), protons (blue) and electrons (magenta). Bottom right panel shows the fit residuals.

The tof-dE/dx method allows to fit the kaon yield close to mid-rapidity. This is not possible using the dE/dx method. Moreover, the kinematic domain in which pion and proton yields can be fitted is enlarged. The results from both methods partly overlap at the highest beam momenta. In these regions the results from the dE/dx method were selected since they have smaller uncertainties.

3.3.3 Probability method

The fit results allow to calculate the probability P_i that a measured particle is of a given type $i = \pi, K, p, e$. For the dE/dx fits (see Eq. 1) one gets:

$$P_i^{dE/dx}(p_{\text{lab}}, p_T) = \frac{\rho_i^{dE/dx}(p_{\text{lab}}, p_T)}{\sum\limits_{i=\pi,K,p,e} \rho_i^{dE/dx}(p_{\text{lab}}, p_T)}, \qquad (6)$$

where ρ_i is the value of the fitted function in a given (p_{lab}, p_T) bin calculated for dE/dx of the particle.

Similarly the tof-dE/dx fits (see Eq. 4) give the particle type probability as

$$P_i^{dE/dx,m^2}(p_{\text{lab}}, p_T) = \frac{\rho_i^{dE/dx,m^2}(p_{\text{lab}}, p_T)}{\sum\limits_{i=\pi,K,p,e} \rho_i^{dE/dx,m^2}(p_{\text{lab}}, p_T)}. \qquad (7)$$
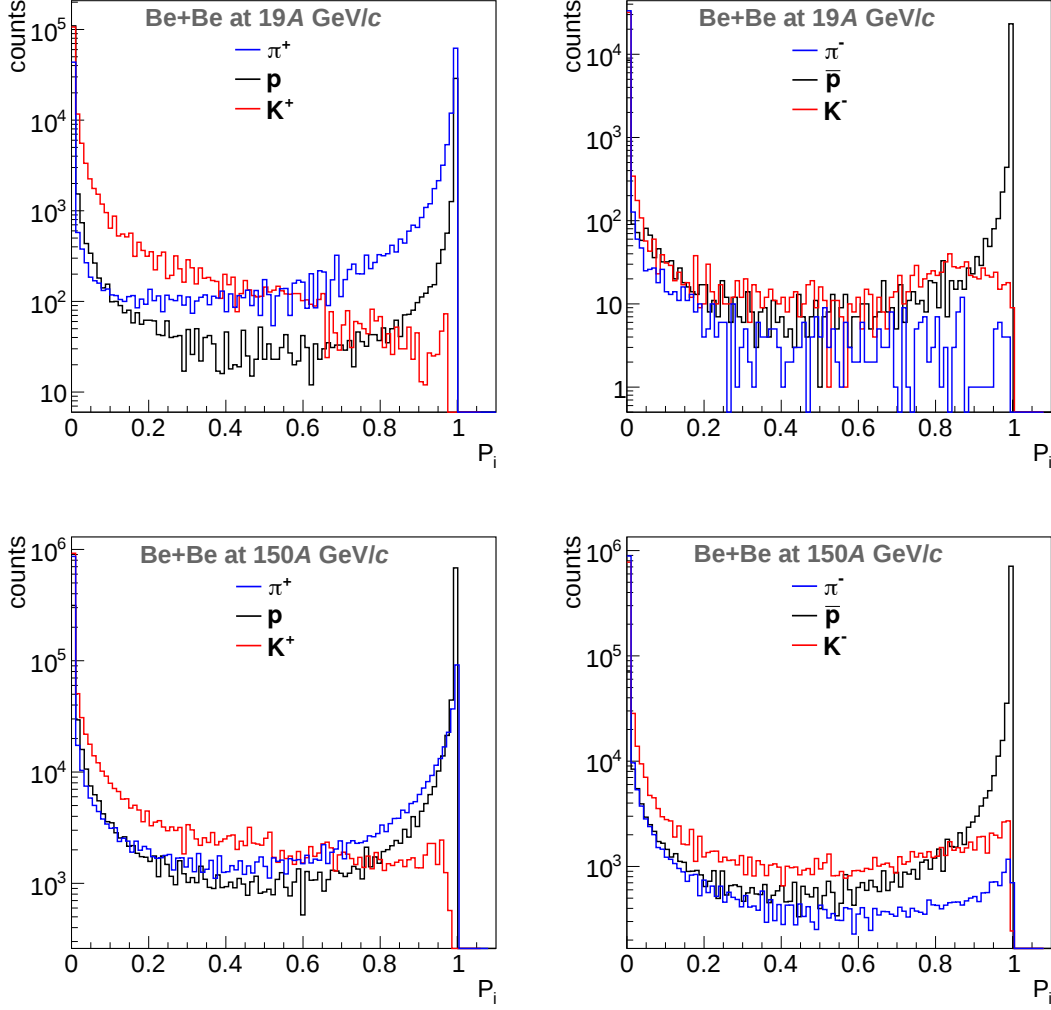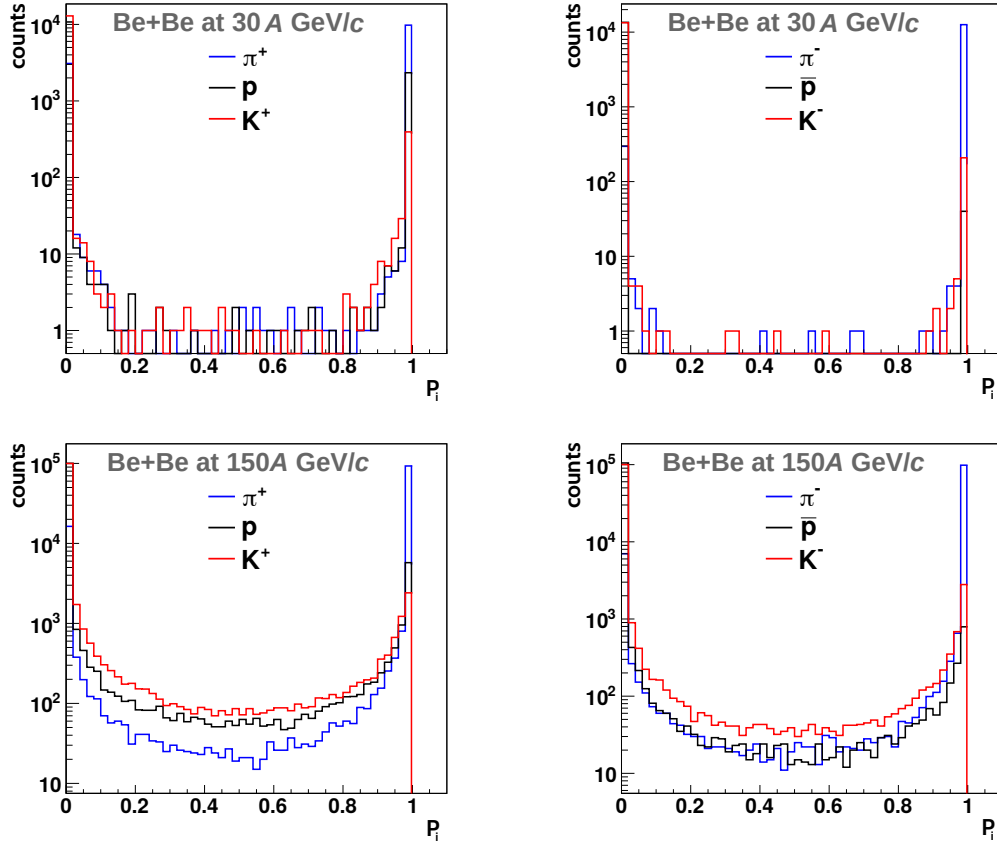
17

Figure 13: Probability of a track being a pion, kaon, proton for positively *(left)* and negatively *(right)* charged particles from dE/dx measurements in PSD selected Be+Be collisions at 19A and 150A GeV/c.

For illustration, particle type probability distributions for positively and negatively charged particles produced in PSD selected Be+Be collisions at 19A and 150A GeV/c are presented in Fig. 13 for the dE/dx fits and in Fig. 14 for the tof-dE/dx fits. In the case of perfect particle type identification the probability distributions in Figs. 13 and 14 will show entries at 0 and 1 only. In the case of incomplete particle identification (overlapping dE/dx or tof-dE/dx distributions) values between these extremes will also be populated.

The probability method allows to transform fit results performed in (p_{lab}, p_T) bins to results in (y, p_T) bins. Hence, for the probability method the mean number of identified particles in a given kinematical bin (e.g. (p_{lab}, p_T)) is given by [27]:

$$n[i]_{dEdx}^{raw}(y, p_T) = \frac{1}{N_{ev}} \sum_{j=1}^{N_{trk}} P_i^{dEdx}(p_{\text{lab}}, p_T),$$

(8)

18

Figure 14: Probability of a track being a pion, kaon, proton for positively (*left*) and negatively (*right*) charged particles from tof-dE/dx measurements in PSD selected Be+Be collisions at $30A$ (*top*) and $150A$ GeV/c (*bottom).*

for the dE/dx identification method and:

$$n[i]_{dEdx,m^2}^{raw}(y,p_T) = \frac{1}{N_{ev}} \sum_{j=1}^{N_{trk}} P_i^{dEdx,m^2}(p_{\text{lab}},p_T), \tag{9}$$

for the tof-dE/dx procedure, where P_i is the probability of particle type i given by Eqs. 6 and 7, j the summation index running over all entries N_{trk} in the bin, N_{ev} is the number of selected events.

Statistical uncertainties of multiplicities calculated with probability method were derived from the variance of the distribution of P_i in the (p_{lab}, p_T) bin:

$$\sigma_{n[i]^{raw}}^2(y,p_T) = \frac{1}{N_{ev}} \left(\sum_{j=1}^{N_{trk}} P_i^j(p_{\text{lab}},p_T)^2 - \left(\sum_{k=1}^{N_{trk}} P_i^j(p_{\text{lab}},p_T) \right)/N_{trk} \right) \tag{10}$$

3.4 Corrections and uncertainties

In order to estimate the true number of each type of identified particle produced in Be+Be interactions a set of corrections was applied to the extracted raw results. These were obtained from a simulation of the NA61/

19

SHINE detector followed by event reconstruction using the standard reconstruction chain. Only inelastic Be+Be interactions were simulated in the target material. The EPOS1.99 model (version CRMC 1.5.3) [16] was selected to generate primary inelastic interactions as it best describes the NA61/SHINE measurements. A GEANT3 based program chain was used to track particles through the spectrometer, generate decays and secondary interactions and simulate the detector response (for details see Ref. [8]). Simulated events were then processed using the standard NA61/SHINE reconstruction chain and reconstructed tracks were matched to the simulated particles based on the cluster positions. The event selection was based on a dedicated simulation of the energy recorded by the PSD (see Sec. 3.1). Corrections depend on the particle identification technique (i.e. dE/dx or tof-dE/dx). Hadrons which were not produced in the primary interaction can amount to a significant fraction of the selected tracks. Thus a special effort was undertaken to evaluate and subtract this contribution. The correction factors were calculated in the same bins of y and p_T as the particle spectra. Bins with a correction factor lower than 1.5 and higher than 4 are caused by low acceptance or high contamination of non primary particles and were rejected.

3.4.1 Corrections for the dE/dx method

The correction factor $c_i^{dEdx}(y, p_T)$ for biasing effects listed in Sec. 3.2.1 items (b) - (g) was calculated as:

$$c_i^{dEdx}(y, p_T) = \frac{n[i]_{gen}^{MC}(y, p_T)}{n[i]_{sel}^{MC}(y, p_T)},$$
(11)

where $n[i]_{gen}^{MC}$ is the number *primary* particles in the (y, p_T) bin for simulated events and $n[i]_{sel}^{MC}$ the number of reconstructed tracks passing all event and track selection cuts. The uncertainty of $c_i^{dEdx}(y, p_T)$ was calculated assuming that the denominator $n[i]_{sel}^{MC}(y, p_T)$ is a subset of the numerator $n[i]_{gen}^{MC}(y, p_T)$ and thus has a binomial distribution. The uncertainty of $c_i^{dEdx}(y, p_T)$ is thus given by:

$$\sigma_{c_i^{dEdx}(y, p_T)} = c_i^{dEdx}(y, p_T) \sqrt{\frac{n[i]_{gen}^{MC}(y, p_T) - n[i]_{sel}^{MC}(y, p_T)}{n[i]_{gen}^{MC} \cdot n[i]_{sel}^{MC}}},$$
(12)

The mean multiplicity for particle type i in the PSD selected events in a (y, p_T) is calculated as:

$$n[i]^{dEdx}(y, p_T) = c_i^{dEdx}(y, p_T) \cdot n[i]_{dEdx}^{raw}(y, p_T).$$
(13)

3.4.2 Corrections for the tof-dE/dx method

The corrections for the tof-dE/dx method were calculated based on simulation and data. The ToF tile efficiency $\varepsilon_{pixel}(p, p_T)$ was calculated from the data in the following way. Each reconstructed track was extrapolated to the ToF walls and if it crossed one of the ToF tiles it was classified as a hit and summed in $n[i]_{tof}$. Moreover, it was accepted as a valid ToF hit, summed in $n[i]_{hit}$, if the signal satisfied quality criteria given in Ref. [26]. Finally, the ToF tile efficiency $\varepsilon_{pixel}(p, p_T)$ was calculated as the ratio of the number of tracks $n[i]_{tof}$ crossing a particular tile to the number of tracks $n[i]_{hit}$ with valid ToF hits. The corresponding efficiency factor $\varepsilon_{pixel}(p, p_T)$ is given by:

$$\varepsilon_{pixel}(p, p_T) = \frac{n[i]_{hit}}{n[i]_{tof}}.$$
(14)

This ToF pixel efficiency factor was used in the MC simulation by weighting each reconstructed MC track passing all event and track selection cuts by the efficiency factor of the corresponding tile. Then, the number of selected MC tracks $n[i]_{sel}^{MC}$ becomes a sum of weights:

$$n[i]_{sel}^{MC} = \sum_{j=1}^{N_{trk}} \varepsilon_{pixel}^{j}(p, p_T). \tag{15}$$

Only hits in working tiles with efficiency higher than 50% were taken into account in the identification and correction procedures. This results in the following correction factor for biasing effects listed in Sec. 3.2.1 items (b)-(g) as well as ToF efficiency, tof-dE/dx method acceptance, secondary interactions and contribution of particles other than *primary*:

$$c_i^{dEdx,m^2}(y, p_T) = \frac{n[i]_{gen}^{MC}}{n[i]_{sel}^{MC}}, \tag{16}$$

where $n[i]_{gen}^{MC}$ is the number *primary* particles in the (y, p_T) bin for simulated events and $n[i]_{sel}^{MC}$ the number of reconstructed tracks passing all event and track selection cuts weighted by the tile efficiency factor $\varepsilon_{pixel}(p, p_T)$ given by Eg. 15.

The uncertainty of $c_i^{dEdx,m^2}(y, p_T)$ was calculated assuming that the denominator $n[i]_{sel}^{MC}(y, pT)$ is a subset of the nominator $n[i]_{gen}^{MC}(y, pT)$ and thus has a binomial distribution. The uncertainty of $c_i^{dEdx,m^2}(y, p_T)$ was calculated as follows:

$$\sigma_{c_i^{dEdx,m^2}}(y, p_T) = c_i^{dEdx,m^2}(y, p_T) \sqrt{\frac{n[i]_{gen}^{MC}(y, p_T) - n[i]_{sel}^{MC}(y, p_T)}{n[i]_{gen}^{MC} \cdot n[i]_{sel}^{MC}}}, \tag{17}$$

The mean multiplicity for particle type i in the PSD selected events in a (y, p_T) bin for the tof-dE/dx method is defined by:

$$n[i]^{dEdx,m^2}(y, p_T) = c_i^{dEdx,m^2}(y, p_T) \cdot n[i]_{dEdx,m^2}^{raw}, \tag{18}$$

3.5 Corrected spectra

Final spectra of different types of hadrons produced in Be+Be interactions are calculated as:

$$\frac{d^2n}{dydp_T} = \frac{1}{\Delta y \cdot \Delta p_T \cdot N_{ev}} \cdot c_i(y, p_T) \cdot n[i]^{raw}(y, p_T), \tag{19}$$

where Δy and Δp_T are the bin sizes, N_{ev} is the total number of accepted events, $n[i]^{raw}$ represents the mean multiplicity for particle type i in the y, p_T bin obtained as $n[i]^{dEdx}$ and $n[i]^{dEdx,m^2}$ for the dE/dx and tof-dE/dx identification method, respectively and finally the correction factor c_i stands for $c_i^{dEdx}(y, p_T)$ (Eq. 11) or $c_i^{dEdx,m^2}(y, p_T)$ (Eq. 16) for the dE/dx and tof-dE/dx identification method, respectively.

Resulting two-dimensional distributions $\frac{d^2n}{dydp_T}$ of $\pi^-, \pi^+, K^-, K^+, p$ and $\bar{p}$ produced in the 20% most *central* Be+Be collisions at different SPS energies are presented in Fig. 15.
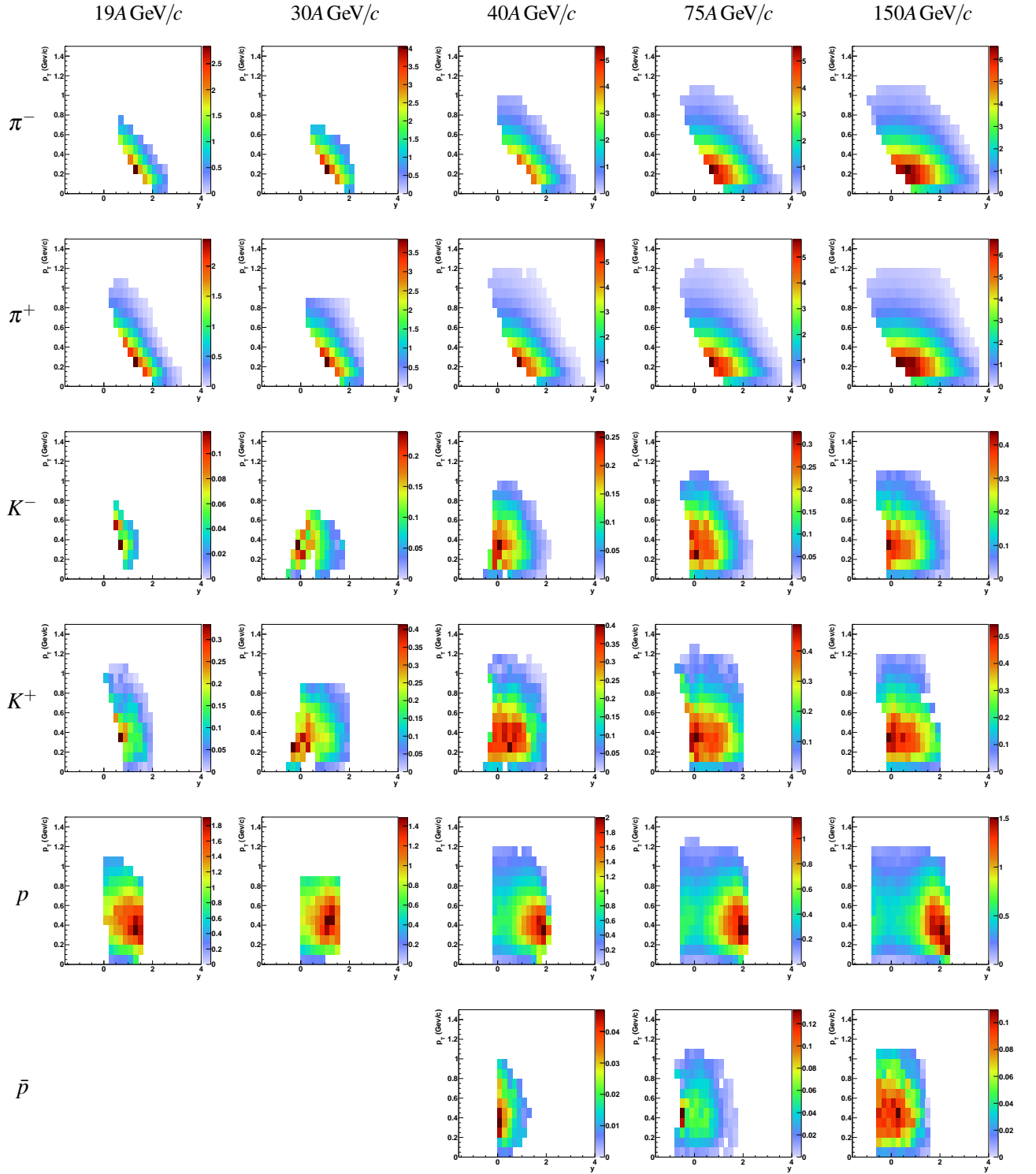
Figure 15: Two-dimensional distributions (y vs. p_T) of yields of π^-, π^+, K^-, K^+, p and $\bar{p}$ produced in the 20% most *central* Be+Be interactions at 19A, 30A, 40A, 75A and 150A GeV/c.

3.5.1 Statistical uncertainties

Statistical uncertainties of yields (Eq. 20) were calculated as:

$$\sigma^2_{stat} = \frac{1}{\Delta y^2 \cdot \Delta p_T^2 \cdot N^2_{ev}} \left(\left(c_i(y,p_T)\sigma_{n[i]^{raw}}(y,p_T) \right)^2 + \left(\sigma_{c_i(y,p_T)} n[i]^{raw} \right)^2 \right), \tag{20}$$

where $\sigma_{n[i]^{raw}}$ (Eq. 10) is the uncertainty of the uncorrected particle multiplicity $n[i]^{raw}$ (Eqs. 8 and 9), $\sigma_{c_i(y,p_T)}$ (Eqs. 12 and 17) denotes the uncertainty of the correction factors $c_i^{dEdx}(y,pT)$ (Eqs. 11) or $c_i^{dEdx,m^2}(y,pT)$ (Eq. 16) for the dE/dx or tof-dE/dx identification method, i is the particle type and N_{ev} the total number of accepted events.

3.5.2 Systematic uncertainties

The contributions to the systematic uncertainty for the dE/dx and tof-dE/dx methods in selected p_T intervals at beam momenta of $19A$ ($30A$) and $150\,A\,\mathrm{GeV}/c$ are presented in Figs. 16-19. Assuming they are uncorrelated, the total systematic uncertainty, also shown in the plots, was calculated as the square root of the sum of squares of the described components.

The considered contributions to systematic uncertainties are listed below:

(i) Event selection:

Systematic uncertainty of final particle yields due to the slightly different procedures of event selection used for data (E_{PSD}) and simulated events (E_F) (see Sec. 3.1).

Systematic uncertainty related to the rejection of events with additional tracks from off-time particles was estimated by changing the width of the time window in which no second beam particle is allowed by $\pm\,1\,\mu s$ with respect to the nominal value of $\pm 4.5\,\mu s$. The maximal difference of the results was assigned as the systematic uncertainty of the selection. This contribution does not affect the results of the $tof-dE/dx$ identification method.

Systematic uncertainty due to the choice of selection window for the z-position of the fitted vertex was estimated by varying the selection criteria for the data and the EPOS 1.99 model in the range of ± 25 cm around the nominal position of the target.

(ii) Track selection:

Systematic uncertainty from the value of the cut on the track impact parameter at the primary vertex was estimated by varying the cut for the data and the EPOS 1.99 model by $\pm 50\%$ around the nominal value.

Systematic uncertainty originating from the requirement on the number of measured points in the magnetic field (minimum number of points in VTPCs and GTPC) was estimated by changing the nominal requirement on the number of measured points by $\pm\,5$ (33% of the standard selection) and $\pm\,10$ (66% of the standard selection) for the dE/dx and $tof-dE/dx$ identification methods, respectively.

(iii) Particle identification:

Uncertainties of the dE/dx identification method were studied and estimated by a 10% variation of the parameter constraints for Eq.1 fitted to the dE/dx spectra.

In case of tof-dE/dx identification, systematic uncertainties were estimated by shifting the mean (x_j and y_j) of the two-dimensional Gaussians (Eq. 4) fitted to the $m^2 - dE/dx$ distributions by $\pm 1\%$.

An additional systematic uncertainty arises for the $tof-$dE/dx method from the quality requirements on the signals registered in the ToF pixels. This systematic uncertainty was estimated by changing the nominal thresholds by $\pm 10\%$.

(iv) Feeddown correction:

The determination of the feeddown correction is based on the EPOS 1.99 model which reasonably describes the available cross section data for strange particles in $p+p$ collisions (see e.g. for K^+, K^- Ref. [9] and for Λ at 158 GeV/c Ref. [28]). Systematic uncertainty comes from the lack of precise knowledge of the production cross section in Be+Be collisions of K^+, K^-, Λ, Σ^+, Σ^-, K^0_s and $\bar{\Lambda}$ in case of pions, and in addition of Σ^+ in case of protons, and $\bar{\Lambda}$ in case of $\bar{p}$.
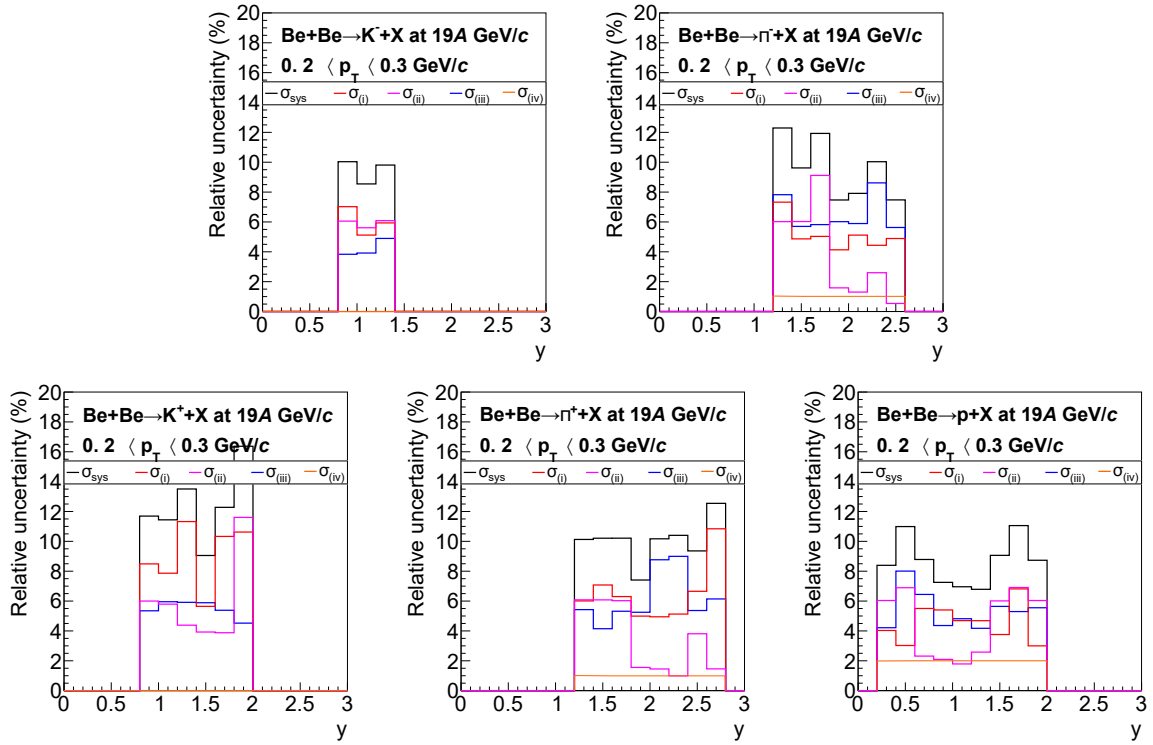
Figure 16: Contributions to the systematic uncertainty of particle spectra obtained from the dE/dx method at 19A GeV/c as a function of rapidity for the transverse momentum interval between $0.2 - 0.3$ GeV/c. $\sigma_{(i)}$ (red lines) refers to event selection $\sigma_{(ii)}$ (magenta lines) to the track selection procedure, $\sigma_{(iii)}$ (blue lines) to the identification technique and $\sigma_{(iv)}$ (orange lines) to the contamination by feeddown from weak decays of strange particles. Black lines, $\sigma_{(sys)}$, show the total systematic uncertainty calculated as the square root of the sum of squares of the components.
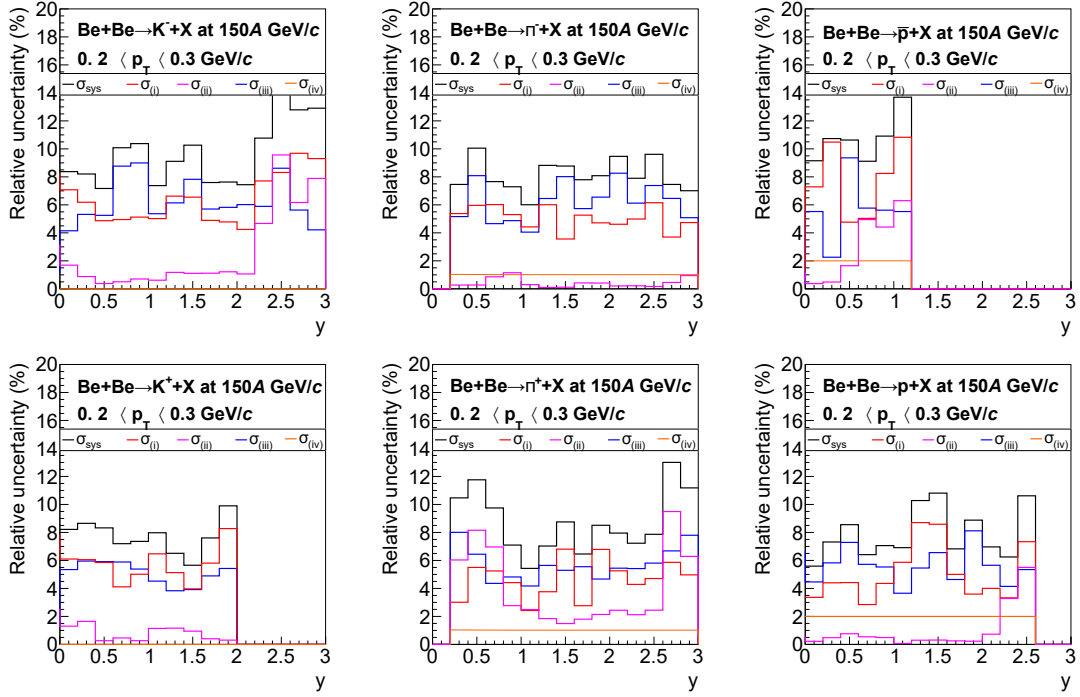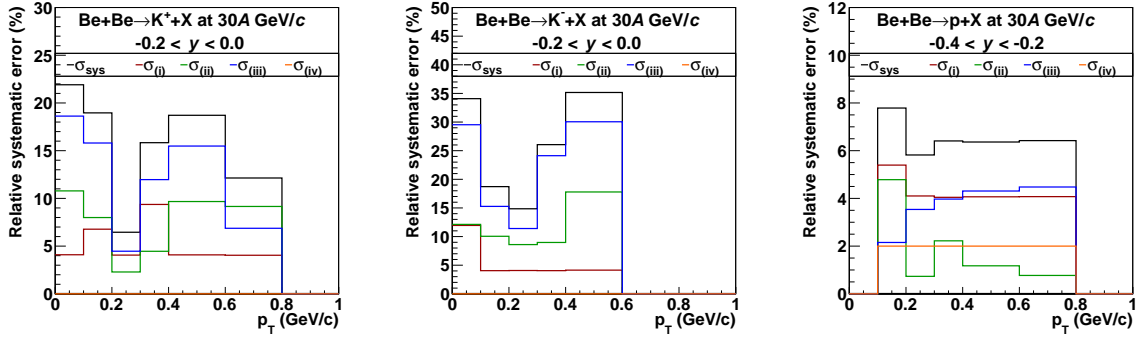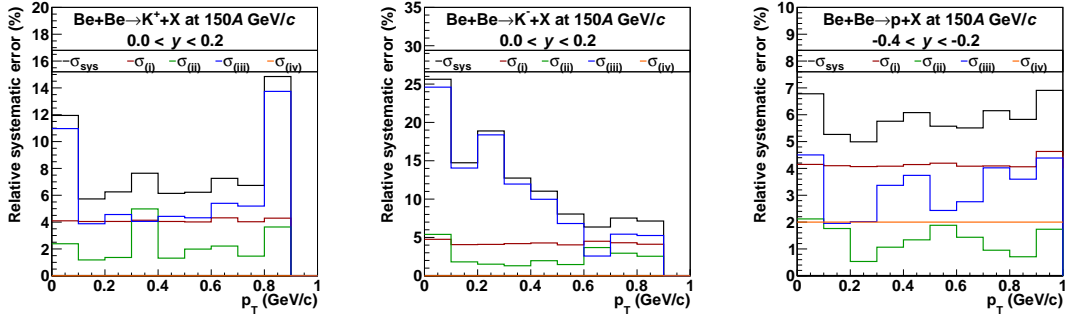
Figure 17: Contributions to the systematic uncertainty of particle spectra obtained from the dE/dx method at 150A GeV/c as a function of rapidity for the transverse momentum interval between 0.2 − 0.3 GeV/c. $\sigma_{(i)}$ (red lines) refers to event selection $\sigma_{(ii)}$ (magenta lines) to the track selection procedure, $\sigma_{(iii)}$ (blue lines) to the identification technique and $\sigma_{(iv)}$ (orange lines) to the contamination by feeddown from weak decays of strange particles. Black lines, $\sigma_{(sys)}$, show the total systematic uncertainty calculated as the square root of the sum of squares of the components.

Figure 18: Contributions to the systematic uncertainty of particle spectra obtained from the tof-dE/dx method at 30A GeV/c as a function of p_T for the rapidity interval -0.2 to 0.0 GeV/c (K^+ and K^-) and -0.4 to -0.2 GeV/c (protons). $\sigma_{(i)}$ (red lines) refers to event selection $\sigma_{(ii)}$ (green lines) to the track selection procedure, $\sigma_{(iii)}$ (blue lines) to the identification technique and $\sigma_{(iv)}$ (orange lines) to the contamination by feeddown from weak decays of strange particles. Black lines, $\sigma_{(sys)}$, show the total systematic uncertainty calculated as the square root of the sum of squares of the components.

25

Figure 19: Contributions to the systematic uncertainty of particle spectra obtained from the tof-dE/dx method at $150A$ GeV/c as a function of p_T for the rapidity interval 0.0 to 0.2 GeV/c (K^+ and K^-) and -0.4 to -0.2 GeV/c (protons). $\sigma_{(i)}$ (red lines) refers to event selection $\sigma_{(ii)}$ (green lines) to the track selection procedure, $\sigma_{(iii)}$ (blue lines) to the identification technique and $\sigma_{(iv)}$ (orange lines) to the contamination by feeddown from weak decays of strange particles. Black lines, $\sigma_{(sys)}$, show the total systematic uncertainty calculated as the square root of the sum of squares of the components.

4 Results

Two dimensional distributions $\frac{d^2n}{dydp_T}$ of π^-, π^+, K^-, K^+, p and $\bar{p}$ produced in the 20% most *central* Be+Be interactions at different SPS energies are presented in Fig. 15. Where available, results from the dE/dx method were used because of their smaller statistical uncertainties. Results from the tof-dE/dx method were taken to extend the momentum space coverage. Reflection symmetry around $y = 0$ was used for $\frac{d^2n}{dydp_T}$ near mid-rapidity (see discussion in Sec.4.2). Empty bins in momentum space (mostly for lower energies) are caused by insufficient acceptance for the identification methods used in the analysis.

4.1 Transverse momentum and transverse mass spectra

Resulting double differential spectra as a function of transverse momentum p_T in intervals of rapidity y of K^+, K^-, π^+, π^-, p and $\bar{p}$ produced at 19A, 30A, 40A, 75A, 150A GeV/c beam momentum are shown in Figs. 20-25. Entries in Fig. 15 below mid-rapidity were reflected in order to fill the gaps in acceptance as far as possible. Spectra in successive rapidity intervals were scaled by appropriate factors for better visibility. Vertical bars on data points correspond to statistical, shaded bands to systematic uncertainties. Systematic uncertainties plotted in the logarithmic scale look small.

Transverse momentum spectra of shown in Figs. 20-25 were parametrized by an exponential function [29, 30]:

$$\frac{d^2n}{dydp_T} = \frac{S\,c^2 p_T}{T^2 + m\,T} \exp(-(m_T - m)/T),\tag{21}$$

where m is the particle mass and S and T are the yield integral and the inverse slope parameter, respectively. The functions (Eq. 21) fitted at mid-rapidity are shown together with the data points for K^+ and K^- in Fig. 26 and for protons and antiprotons in Fig. 27.

The fitted inverse slope parameter is plotted in Fig. 28 as a function of the rapidity. The value of T results from an interplay of the kinetic freeze-out temperature when final state rescattering stops as well as of the radial expansion flow. Thus the p_T spectra need not show a strictly exponential decrease. Note that
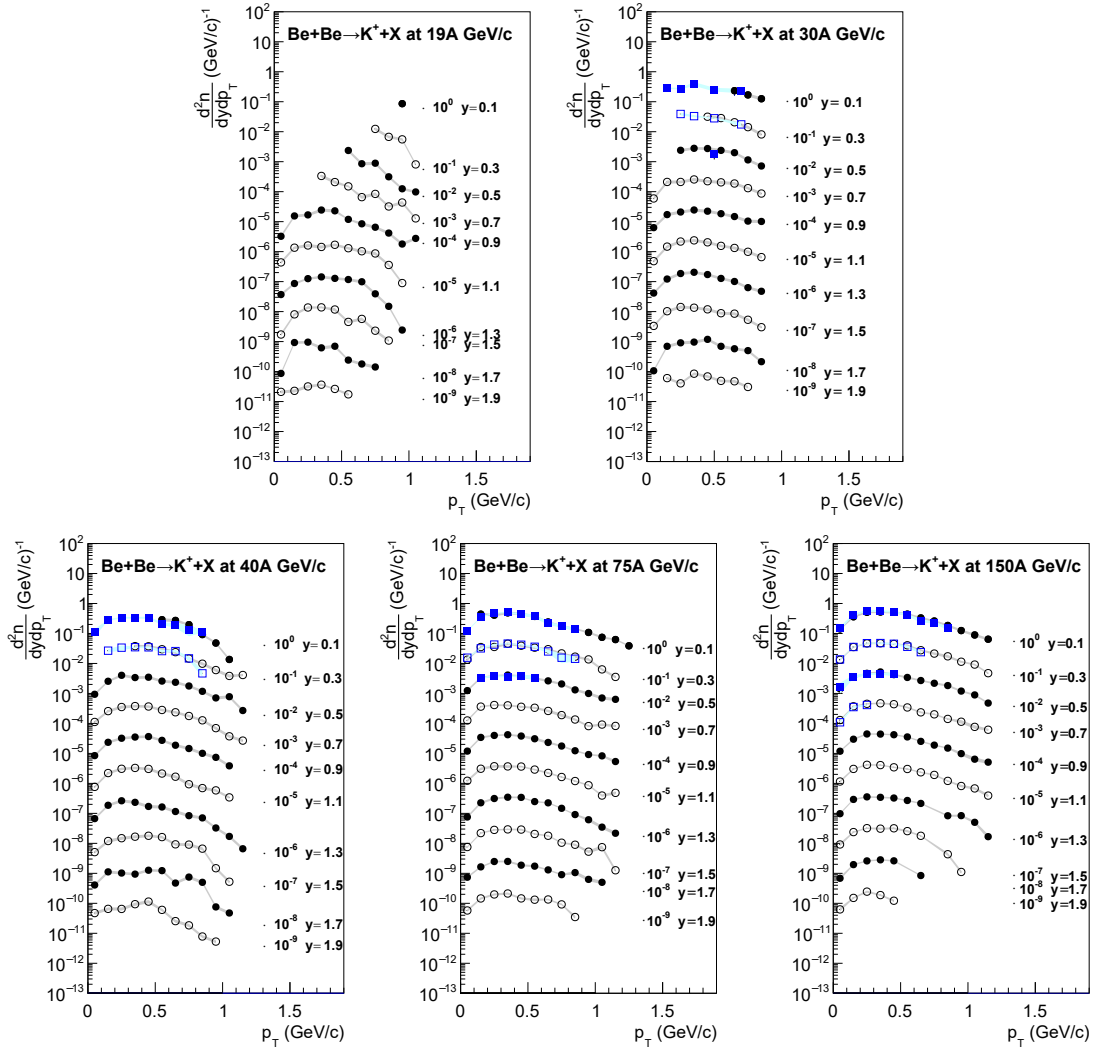
Figure 20: Transverse momentum spectra in rapidity slices of K^+ produced in the 20% most *central* Be+Be collisions. Rapidity values given in the legends correspond to the middle of the corresponding interval. Black dots (blue squares) show results of the dE/dx (tof-dE/dx) analysis, respectively. Shaded bands show systematic uncertainties.
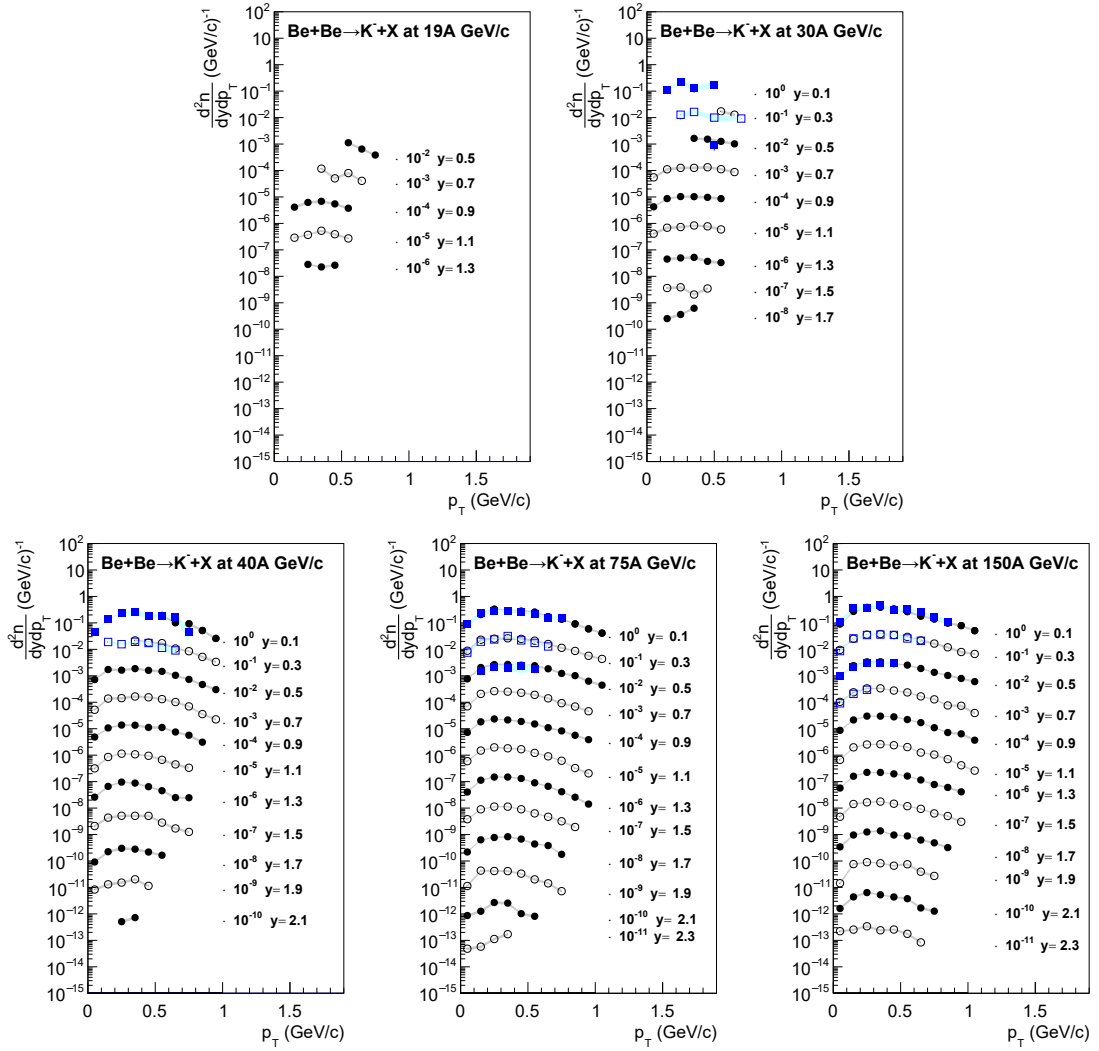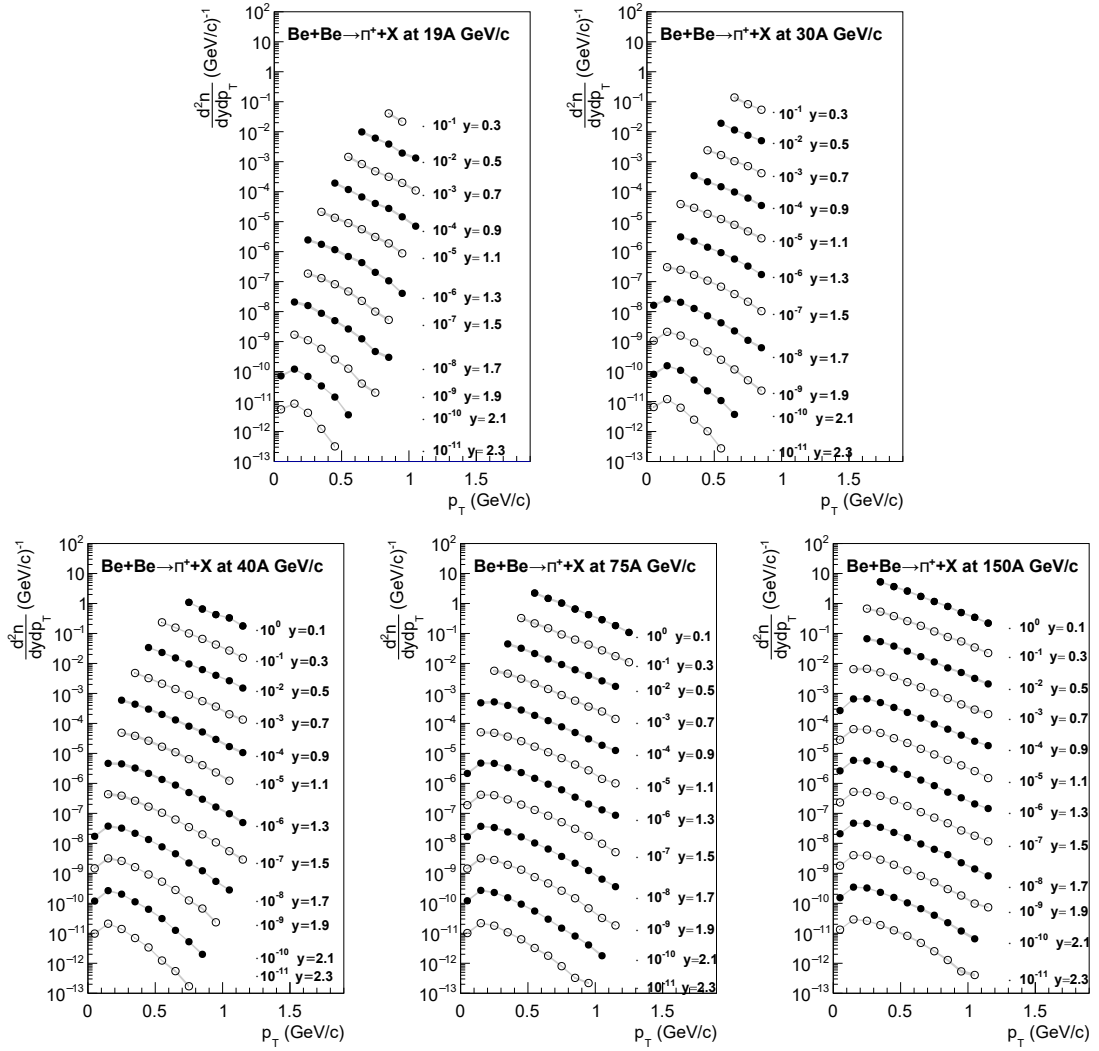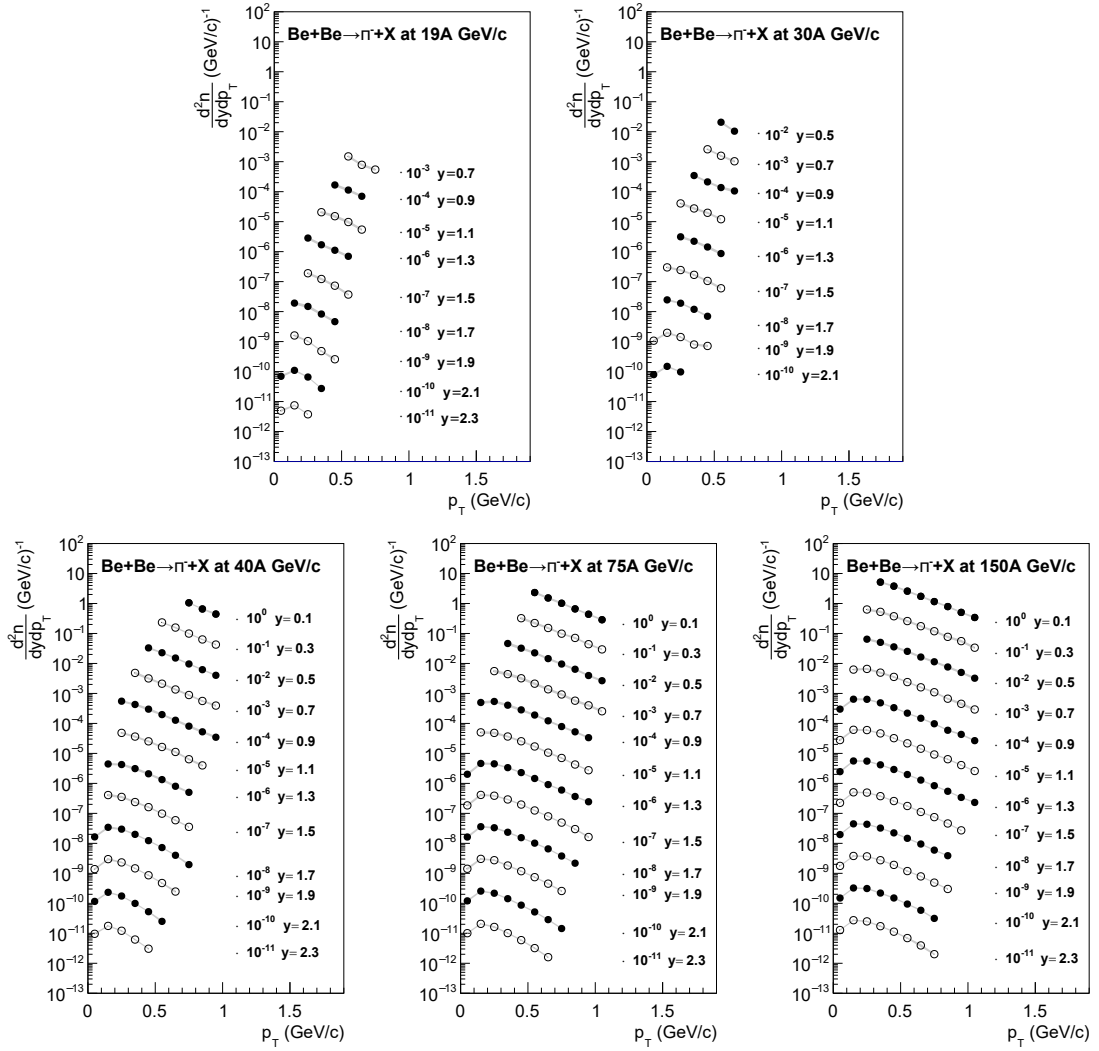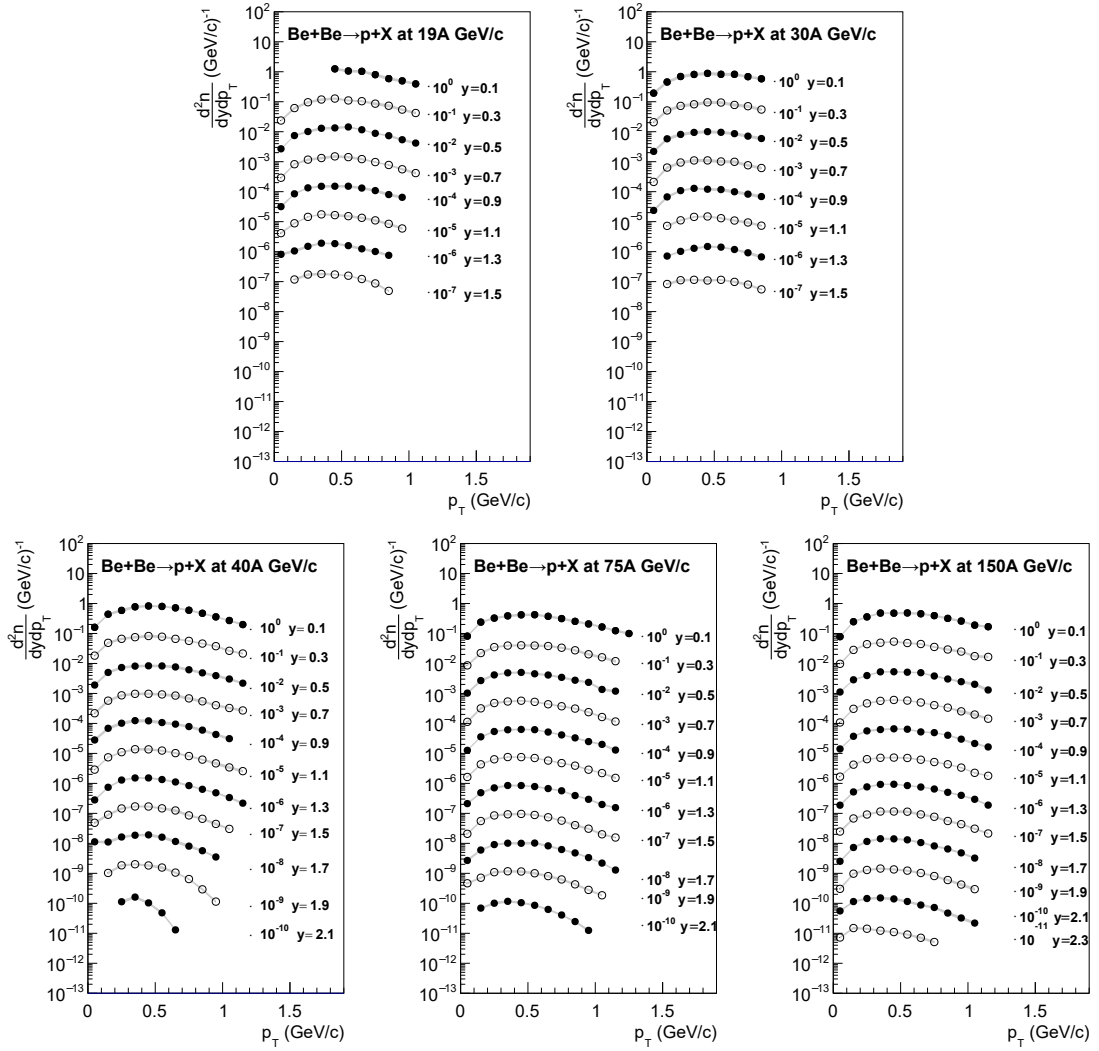
Figure 21: Transverse momentum spectra in rapidity slices of K^- produced in the 20% most *central* Be+Be collisions. Rapidity values given in the legends correspond to the middle of the corresponding interval. Black dots (blue squares) show results of the dE/dx (tof-dE/dx) analysis, respectively. Shaded bands show systematic uncertainties.

Figure 22: Transverse momentum spectra in rapidity slices of π^+ produced in the 20% most *central* Be+Be collisions. Rapidity values given in the legends correspond to the middle of the corresponding interval. Presented results were obtained with the dE/dx analysis method. Shaded bands show systematic uncertainties.
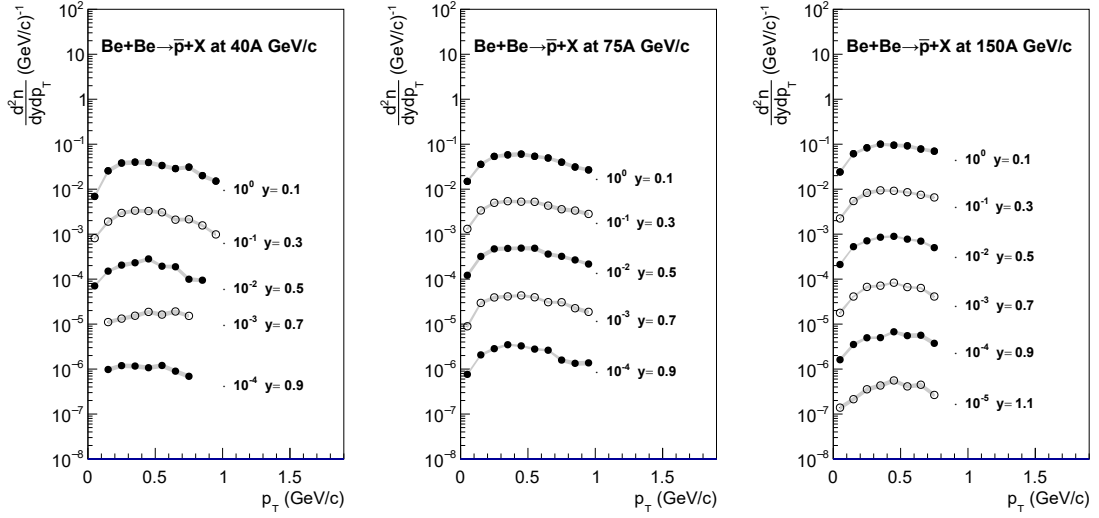
Figure 23: Transverse momentum spectra in rapidity slices of π^- produced in the 20% most *central* Be+Be collisions. Rapidity values given in the legends correspond to the middle of the corresponding interval. Presented results were obtained with the dE/dx analysis method. Shaded bands show systematic uncertainties.
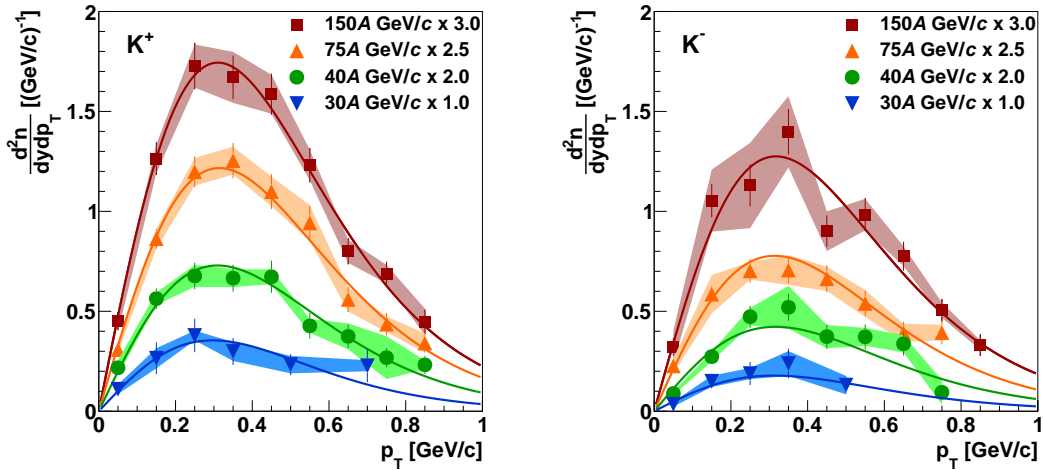
Figure 24: Transverse momentum spectra in rapidity slices of protons produced in the 20% most *central* Be+Be collisions. Rapidity values given in the legends correspond to the middle of the corresponding interval. Presented results were obtained with the dE/dx analysis method. Shaded bands show systematic uncertainties.

Figure 25: Transverse momentum spectra in rapidity slices of antiprotons produced in the 20% most *central* Be+Be collisions. Rapidity values given in the legends correspond to the middle of the corresponding interval. Presented results were obtained with the dE/dx analysis method. Shaded bands show systematic uncertainties.

Figure 26: Transverse momentum spectra of K^+ (*left*) and K^- (*right*) mesons produced in $0 < y < 0.2$ (-0.2 $< y < 0.0$ for $30A$ GeV/c) in the 20% most *central* Be+Be collisions. Colored lines represent the fitted function (Eq. 21).

results are only plotted for those rapidity intervals for which there were more than 6 data points in the p_T-distribution.

Rapidity spectra dn/dy of K^+ and K^- were obtained by integration of the transverse momentum distributions shown in Fig. 26. Both dn/dy and the corresponding inverse slope parameter T at mid-rapidity are tabulated in Table 3.

A step-like structure in the energy dependence of the inverse slope parameter T of kaons at mid-rapidity
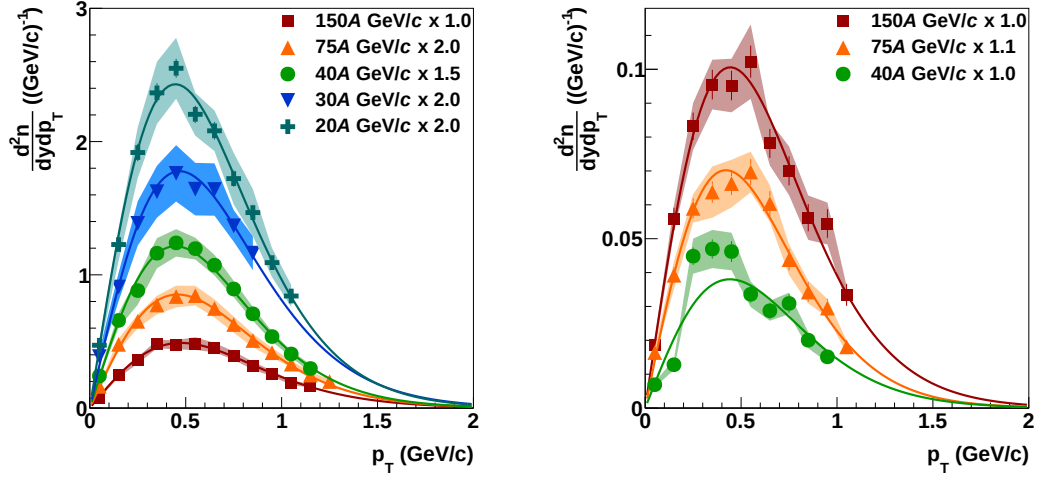
Figure 27: Transverse momentum spectra of protons (*left*) and antiprotons (*right*) produced in 0 <*y* < 0.2 in the 20% most *central* Be+Be collisions. Colored lines represent the fitted function (Eq. 21).

Table 3: Mid-rapidity K^+ and K^- multiplicities dn/dy and inverse slope parameters T at in 0 <*y* < 0.2 (-0.2 <*y* <0.0 for 30A GeV/c) produced in the 20% most *central* Be+Be collisions. For each value the statistical and systematic uncertainties are given as the first and second uncertainty contribution, respectively.

	K^+		K^-	
	$\left(\frac{dn}{dy}\right)_{y\approx 0}$	T_{K^+}	$\left(\frac{dn}{dy}\right)_{y\approx 0}$	T_{K^-}
30A GeV/c	0.209±0.025±0.021	0.152±0.016 ±0.012	0.111±0.019±0.015	0.167±0.023±0.014
40A GeV/c	0.220±0.009±0.022	0.164±0.007±0.006	0.136±0.007±0.020	0.170±0.011±0.012
75A GeV/c	0.288±0.009±0.021	0.168±0.006±0.005	0.182±0.007±0.019	0.168±0.009±0.005
150A GeV/c	0.338±0.008±0.028	0.165±0.005±0.007	0.254±0.008±0.036	0.171±0.007±0.012

was predicted [32] at the onset of deconfinement (*step*). In this scenario it is caused by the softness of the equation of state of the mixed phase of hadrons and partons stalling the expansion of the initial state with rising energy density. Kaon p_T spectra are well described by a simple exponential because in contrast to pion p_T spectra they are not affected strongly by resonance decay products. As seen in Fig. 29 from a compilation of published results such a step is observed in central collisions of heavy nuclei (Au and Pb) in the SPS energy range which is consistent with the onset of the phase transition [11, 12]. The new NA61/SHINE measurements from *central* Be+Be collisions are similar to published results from inelastic p+p interactions. This indicates that not much expansion flow is created in the small Be+Be collision system at SPS energies. Although there appears to be a similar step feature, the values of T are much smaller than the ones from collisions of heavy nuclei. The intriguing similarity between the energy dependence of T between p+p and Pb+Pb collisions is discussed in detail in Ref. [10].
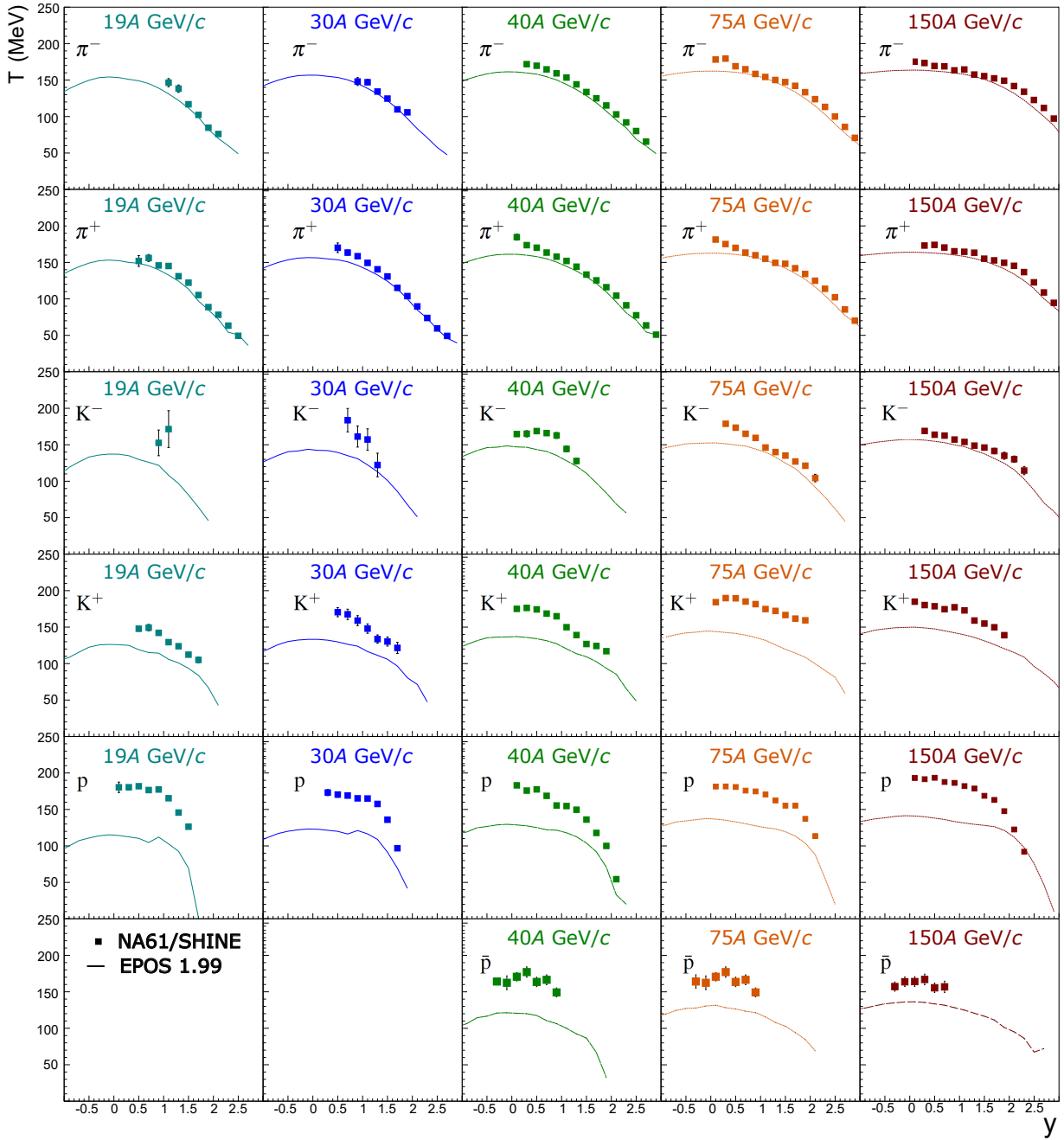
Figure 28: Inverse slope parameter *T* of the p_T distributions as function of rapidity *y* fitted with Eq. 21 in the full available p_T range. Results for the 20% most *central* Be+Be collisions at beam momenta of 19*A*, 30*A* 40*A*, 75*A* and 150*A* GeV/*c*. Only statistical uncertainties are shown, systematic uncertainties are estimated at about 10%. Dashed curves show predictions of the EPOS [16, 31] model for comparison.
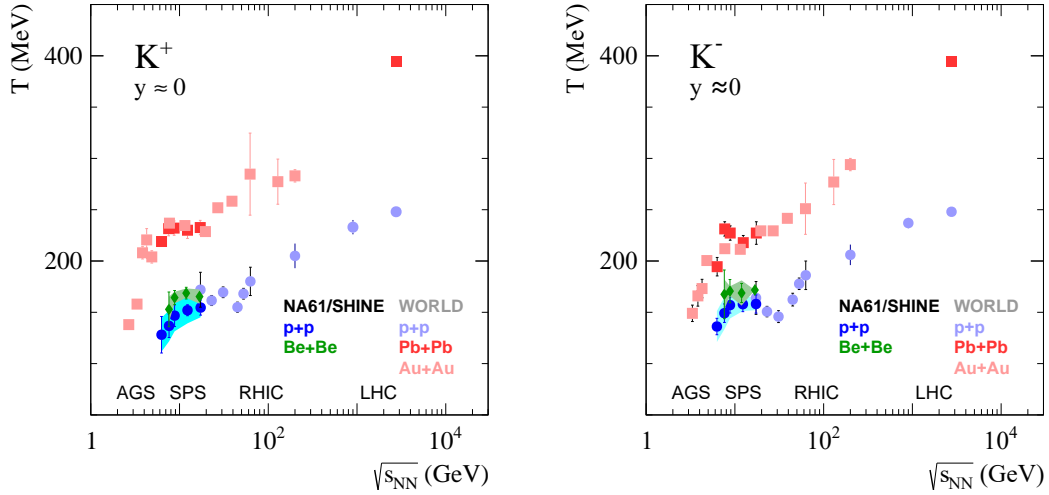
34

Figure 29: The energy dependence of the inverse slope parameter of p_T spectra at mid-rapidity of positively (*left*) and negatively (*right*) charged K mesons for *central* Be+Be, Pb+Pb and Au+Au collisions as well as inelastic $p+p$ interactions. Both statistical (vertical bars) and systematic uncertainties (shaded bands) are shown.

4.2 Rapidity spectra and mean multiplicities

Figure 30 presents rapidity spectra for all studied particle species at all available collision energies. Measurements of the π^- rapidity distributions employing the h^- method indicated slight forward-backward asymmetry [4]. The acceptance for particle identification does not extend into the backward hemisphere making such a test impossible. The forward-backward asymmetry of π^- rapidity spectra reported in Ref. [4] was at the level of 5%. Since this is smaller than the systematic uncertainty no correction was applied. In fact, Gaussian functions provide a good description for all particle types except for protons. The latter exhibit a strong leading particle effect. Mean forward multiplicities (protons excepted), were obtained by summing the measured points and adding an extrapolation estimated from the fitted Gaussian functions which are shown by the curves in Fig. 30. Assuming forward-backward symmetry total mean multiplicities were calculated and are summarized in Table 5.

The simplest model of nucleus-nucleus collisions, the Wounded Nucleon Model [20], suggests that total produced particle multiplicities scale approximately with the respective ratios of wounded nucleons. This ratio was derived using the EPOS model and the NA61/SHINE *centrality* selection procedure for Be+Be collisions with the 20% smallest number of wounded nucleons (see Sec. 3.1) and inelastic $p+p$ collisions Ref. [10]. The resulting ratio of about 4 is close to the experimental ratios calculated from the total multiplicities listed in Table 5 for Be+Be and Ref. [10] for $p+p$ interactions.

The determination of the mean multiplicity is more complicated for protons due to the rapid rise of the yield towards beam rapidity and the lack of measurements in this region. A comparison of the rapidity distributions obtained in this analysis with predictions of the UrQMD [33,34], EPOS [16,31], AMPT [35–37], PHSD 4.0 [38,39] and SMASH 1.6 [40,41] models at 40A and 150A GeV/c beam momentum is shown in Fig. 31. Note that protons with $p_T \approx 0$ and beam rapidity are assumed to be spectator protons and rejected in the model calculations. To determine the mean proton multiplicity one may calculate extrapolation factors from the models as the ratio of mean multiplicity to that in the region covered by the measurements.

The multiplicity of protons in the region of measurements and the extrapolation factor obtained from the EPOS model are given in Table 4. Mean proton multiplicities are not provided since the values will be strongly model dependent.

The total multiplicities for all studied particle species are plotted as a function of collision energy in Fig. 32 and compared to the corresponding results from inelastic $p+p$ interactions. Particle yields in Be+Be collisions are higher by approximately a factor of four consistent with expectations from the wounded nucleon model.

Table 4: Yield of protons in the rapidity acceptance of measurements, the extrapolation factor to mean multiplicity based on the EPOS model.

	$\langle p_{y_{acc}} \rangle$	y_{acc}	$(\langle p_{y_{acc}} \rangle / \langle p_{y>0} \rangle)_{\text{EPOS}}$
$19A$ GeV/c	$1.657 \pm 0.031 \pm 0.191$	$0 < y < 1.5$	69%
$30A$ GeV/c	$1.312 \pm 0.014 \pm 0.063$	$0 < y < 1.5$	54%
$40A$ GeV/c	$1.878 \pm 0.011 \pm 0.057$	$0 < y < 2.1$	78%
$75A$ GeV/c	$1.232 \pm 0.008 \pm 0.026$	$0 < y < 2.1$	60%
$150A$ GeV/c	$0.928 \pm 0.029 \pm 0.060$	$0 < y < 2.3$	48%

Table 5: Mean multiplicities of K^+, K^-, π^+, π^-, protons and antiprotons produced in the 20% most *central* Be+Be collisions. For each value the statistical and systematic uncertainties are given as a first and second uncertainty contribution respectively.

	$\langle K^+ \rangle$	$\langle K^- \rangle$
$19A$ GeV/c	$0.308 \pm 0.025 \pm 0.040$	$0.131 \pm 0.030 \pm 0.041$
$30A$ GeV/c	$0.522 \pm 0.044 \pm 0.052$	$0.220 \pm 0.046 \pm 0.046$
$40A$ GeV/c	$0.665 \pm 0.012 \pm 0.071$	$0.256 \pm 0.011 \pm 0.042$
$75A$ GeV/c	$0.904 \pm 0.027 \pm 0.104$	$0.464 \pm 0.019 \pm 0.046$
$150A$ GeV/c	$1.067 \pm 0.012 \pm 0.108$	$0.628 \pm 0.011 \pm 0.062$
	$\langle \pi^+ \rangle$	$\langle \pi^- \rangle$
$19A$ GeV/c	$5.323 \pm 0.340 \pm 0.998$	$5.021 \pm 0.321 \pm 1.129$
$30A$ GeV/c	$6.807 \pm 0.200 \pm 0.605$	$6.333 \pm 0.321 \pm 0.713$
$40A$ GeV/c	$8.449 \pm 0.208 \pm 0.705$	$8.033 \pm 0.419 \pm 0.745$
$75A$ GeV/c	$9.581 \pm 0.078 \pm 0.756$	$9.312 \pm 0.099 \pm 0.754$
$150A$ GeV/c	$12.344 \pm 0.085 \pm 0.975$	$11.817 \pm 0.086 \pm 0.957$
	$\langle \overline{p} \rangle$	
$19A$ GeV/c	-	
$30A$ GeV/c	-	
$40A$ GeV/c	$0.034 \pm 0.004 \pm 0.006$	
$75A$ GeV/c	$0.084 \pm 0.004 \pm 0.009$	
$150A$ GeV/c	$0.146 \pm 0.006 \pm 0.015$	

4.3 K/π ratio

The K/π ratio at SPS energies was shown to be a good measure of the strangeness to entropy ratio [42] which is different in the confined phase (hadrons) and the QGP (quarks, anti-quarks and gluons). A maximum (*horn*) and a subsequent plateau in the energy dependence of the K^+/π^+ ratio was observed

by the NA49 experiment in the SPS energy range (see Fig. 33) in central Pb+Pb collisions [11, 12] and interpreted as one of the indications of the onset of deconfinement [32].

The NA61/SHINE experiment studies the evolution of this signal with respect to the size of the collision system in order to find when deconfinement starts occurring. In $p+p$ interactions and Be+Be collisions the $K^{\pm}$ and π^- yield can be measured by NA61/SHINE over all of phase space. This is not possible for the π^+ yield which has to be derived from the π^- yield using an isospin correction. Be+Be collisions, however, are isospin symmetric and therefore the mean multiplicities of π^+ and π^- have to be the same. The π^- yields for the 20% most *central* Be+Be collisions were calculated by scaling the π^- multiplicity published in Ref. [4] by the ratio of $\langle W \rangle$ for the 20% (see Table 2) and the 5% most *central* Be+Be collisions Ref. [4]. The results for the energy dependence of the K^+/π^+ ratio from the 20% most *central* Be+Be collisions are shown in Fig. 33 together with measurements in inelastic $p+p$, central Pb+Pb collisions and other reactions. The results from Be+Be collisions do not yet deviate from those in $p+p$ reactions and are about a factor two lower for the total yield ratio than the values found in central Pb+Pb and Au+Au collisions. In particular, no *horn* structure is observed for the small collision systems.

5 Comparison with models

This subsection compares observables, sensitive to the onset of deconfinement, between measurements and model predictions. The EPOS 1.99 [43], URQMD 3.4 [33, 34], AMPT 1.26 [35–37], PHSD 4.0 [38, 39] and SMASH 1.6 [40, 41] models were chosen for this study. In EPOS the reaction proceeds from the excitation of strings according to Gribov-Regge theory to string fragmentation into hadrons. URQMD starts with a hadron cascade based on elementary cross sections for resonance production which either decay (mostly at low energies) or are converted into strings which fragment into hadrons (mostly at high energies). AMPT uses the heavy ion jet interaction generator (HIJING) for generating the initial conditions, Zhang's parton cascade for modeling partonic scatterings and the Lund string fragmentation model or a quark coalescence model for hadronization. PHSD is a microscopic offshell transport approach that describes the evolution of a relativistic heavy-ion collision from the initial hard scatterings and string formation through the dynamical deconfinement phase transition to the quark-gluon plasma as well as hadronization and the subsequent interactions in the hadronic phase. SMASH uses the hadronic transport approach where the free parameters of the string excitation and decay are tuned to match the experimental measurements in inelastic $p+p$ collisions. Selection of events in all model calculations follows the procedure for central collisions to which experimental results correspond to, see Sec. 3.1. This is particularly important when comparisons of yields with measurements are to be performed.

Comparisons of the p_T spectra at midrapidity and rapidity spectra of K^+, K^- and π^- in the 20% most *central* Be+Be collisions at $150A\,\text{GeV}/c$ are shown in Figs. 34 and 35 respectively. Positively charged kaon p_T distributions are overpredicted by AMPT, PHSD and EPOS, whereas URQMD and SMASH predictions are closer to the measurements (Fig. 34 (*top-left*)). In the case of negatively charged K mesons (Fig. 34 (*top-right*)), EPOS next to SMASH describes p_T the distribution well, while URQMD, PHSD and AMPT overestimate the measured spectrum. For π^- one finds a similar behaviour (Fig. 34 (*bottom-left*)). In the case of protons (Fig. 34 (*bottom-right*)), again all models overestimate the p_T spectrum. Moreover, EPOS, SMASH and PHSD predict narrower p_T spectra than measured, which result in smaller value of inverse slope parameter than the one obtained by the data fit (see Figs. 28 and 34).

Predictions for the rapidity distributions are too high for all models (Figs. 35 and 31).

The measurements of the inverse slope parameter T in midrapidity in the 20% most *central* Be+Be collisions are shown versus collision energy for K^+ and K^- in Fig. 36 (*top*) together with model predictions. Except for AMPT the predictions cluster around the measurements. UrQMD and PHSD feature a hadron rescattering phase as the last step of the system's evolution. The values of T for π^- shown in Fig. 36 (*bottom-left*) are well reproduced by EPOS, UrQMD and SMASH whereas the predictions of AMPT and PHSD are too high by 30 - 50 MeV. The limited range of studied beam momentum does not allow a definite conclusion on a possible *step* structure. UrQMD predictions for inverse slope parameter of protons reproduce the experimental data quite well. AMPT model significantly overestimates T value for p, while PHSD, EPOS and SMASH present opposite tendency. Comparison of T as a function of y with EPOS predictions is presented in Fig. 28 for K^+, K^-, π^+, π^-, p and $\overline{p}$. In general, EPOS underestimates T for all types of identified hadrons except pions, for which simulation follows the experimental results.

Finally, the energy dependence of the ratios of kaon to pion yields are compared to model predictions. Figure 37 shows the mid-rapidity results for K^+/π^+ (left) and K^-/π^- (right), respectively. Figure 38 displays the ratios of total mean multiplicities. Unlike particle yields, particle ratios are not sensitive to the details of the event selection assuming that the shapes of the spectra do not change significantly in the studied centrality range. For K^+/π^+ EPOS, UrQMD and SMASH provide a good description whereas AMPT and PHSD overpredict the data. For K^-/π^- all models are close to the experimental results.

A detailed investigation of the effects included in the models and their impact on the predictions of the experimental results is beyond the scope of this paper. However, the new NA61/SHINE measurements provide useful input for future refinements of the models.
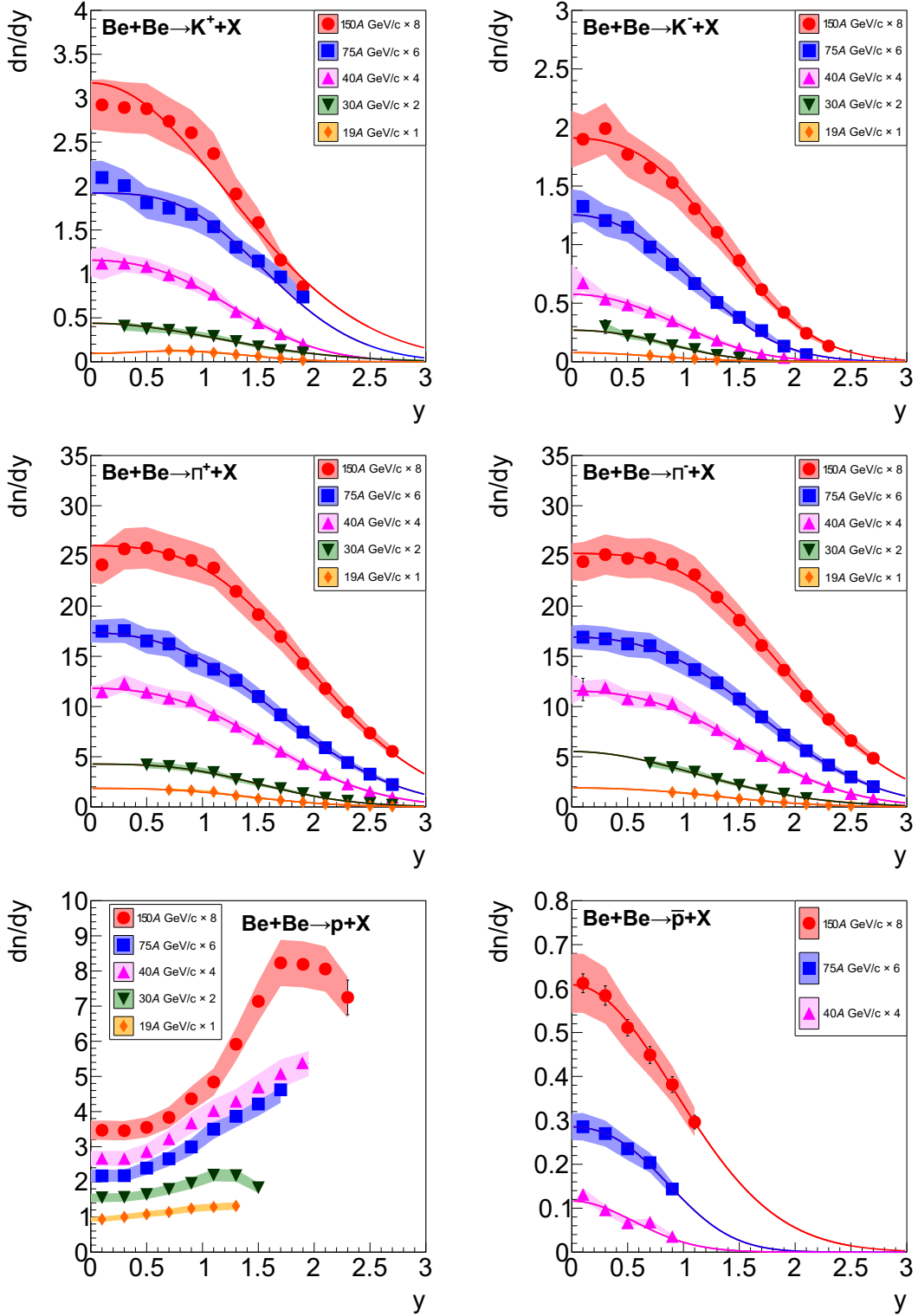
Figure 30: Rapidity spectra of K^+, K^-, π^+, π^-, protons and antiprotons produced in the 20% most *central* Be+Be collisions. Curves depict Gaussian fits used to determine mean multiplicities. Spectra for different beam momenta were scaled by the following factors for better visibility: 150A GeV/c by factor 8, 75A GeV/c by factor 6, 40A GeV/c by factor 4, 30A GeV/c by factor 2 and 19A GeV/c by factor 1.
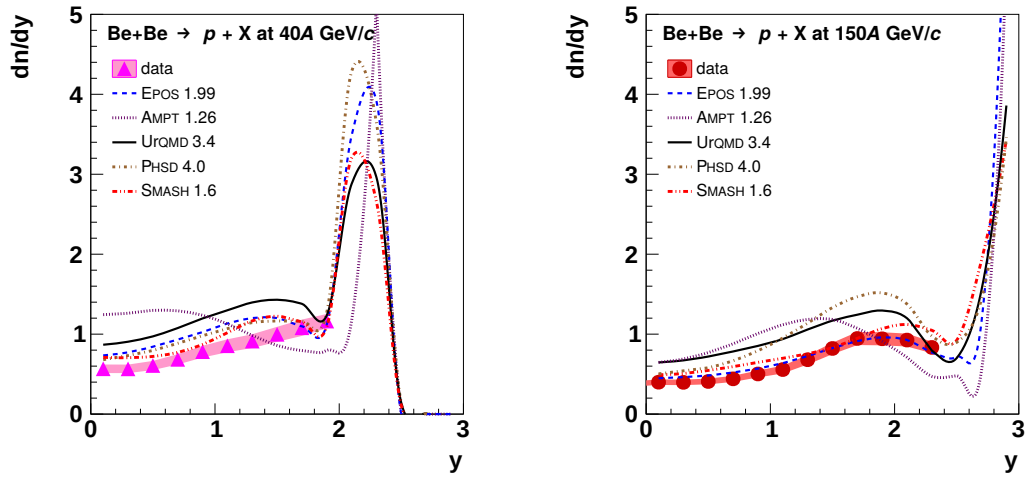
Figure 31: Proton rapidity distribution in the 20% most *central* Be+Be collisions at 40*A* and 150*A* GeV/*c* compared with predictions of the EPOS 1.99 [16, 31] (blue dashed line), UrQMD 3.4 [33, 34] (black solid line), AMPT 1.26 [35–37] (violet dotted line), PHSD 4.0 [38, 39] (brown dashed-dotted line) and SMASH 1.6 (red dashed-double dotted line) [40, 41] models.
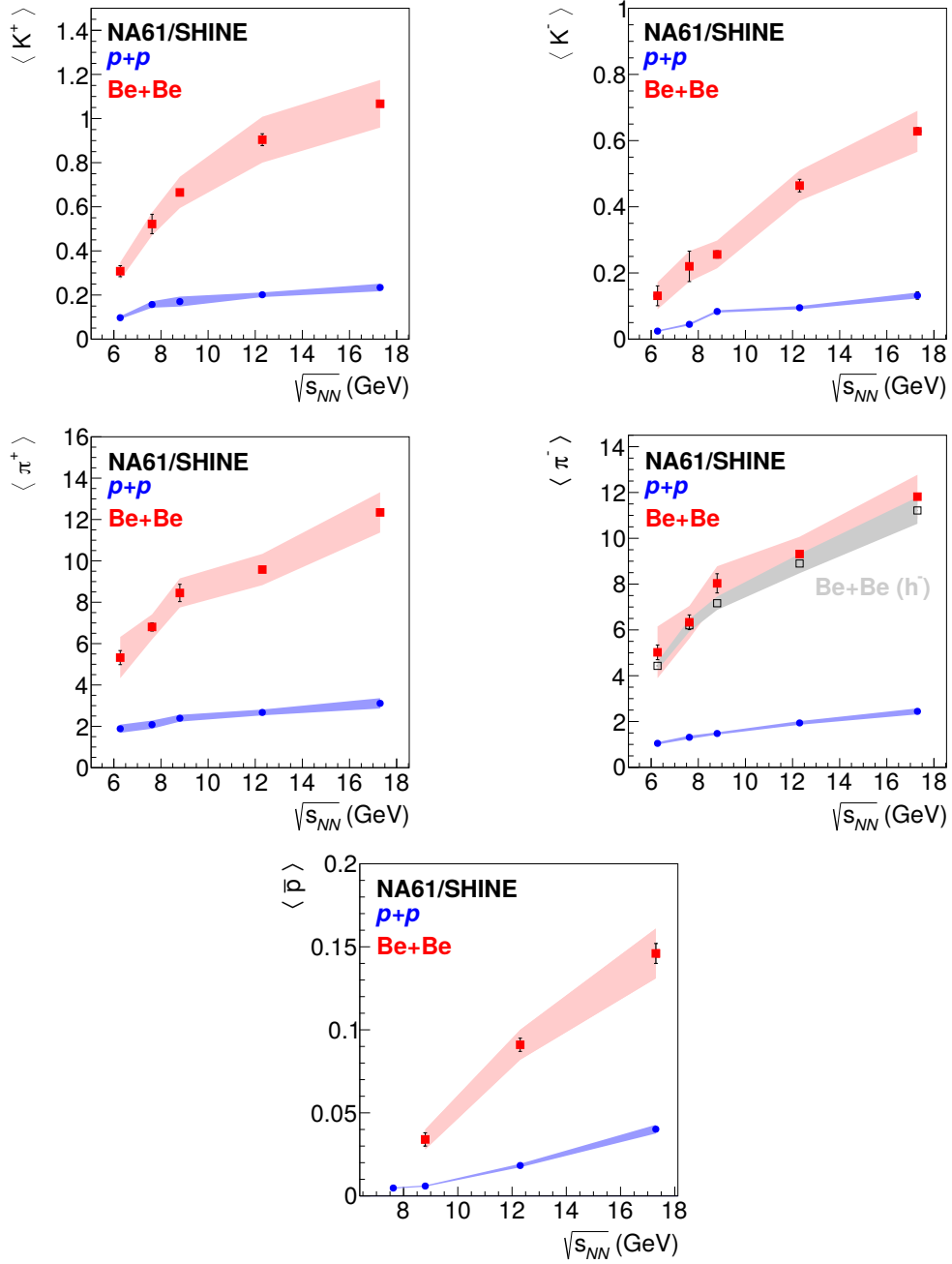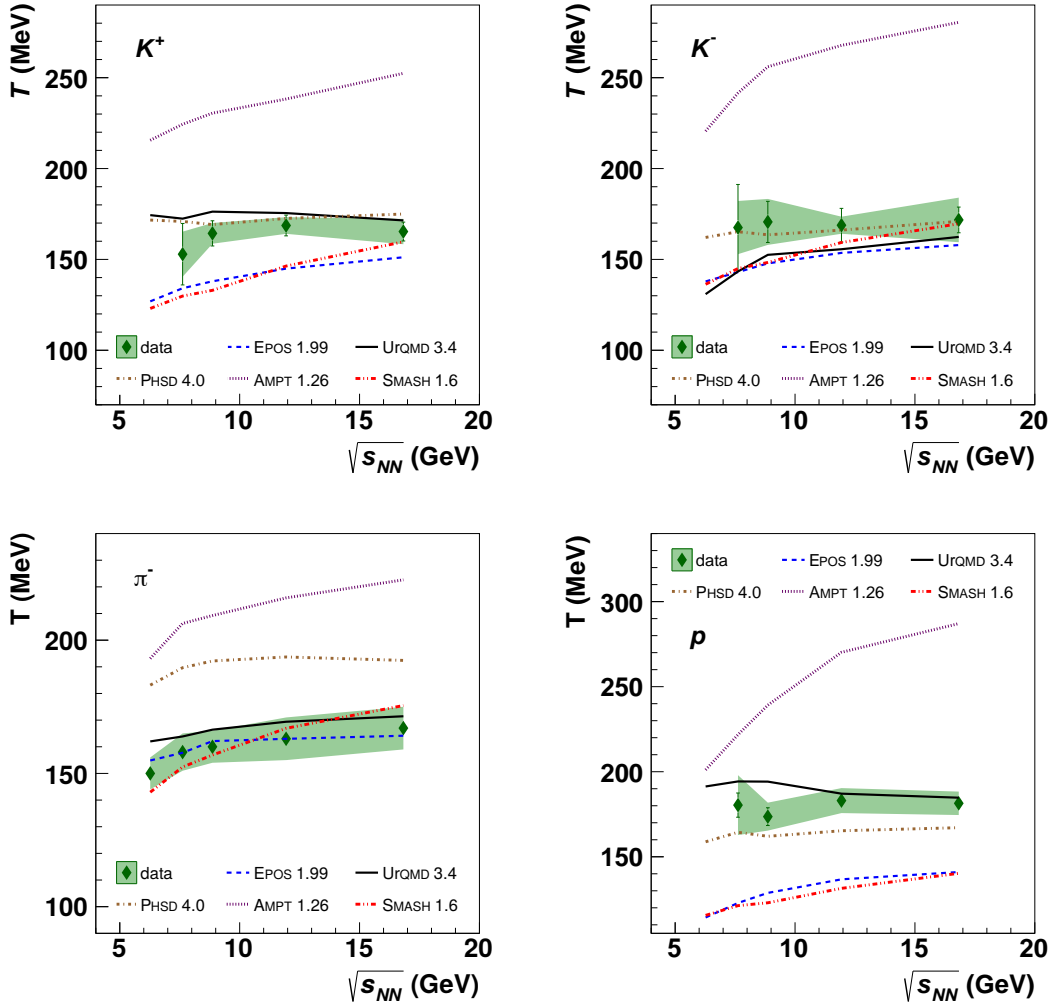
Figure 32: Collision energy dependence of mean multiplicities of K^+, K^-, π^+, π^-, protons and antiprotons produced in the 20% most *central* Be+Be collisions. Results from inelastic $p+p$ interactions [8, 9] are plotted for comparison. Both statistical (vertical bars) and systematic uncertainties (shaded bands) are shown. Gray points and band correspond to π^- results obtained via h^- method. Results for $\langle \pi^- \rangle$ obtained using the h^- method [4] taking into account backward-forward asymmetry of the rapidity distribution. They were scaled from 5% *centrality* to 20% based on the ratio of wounded nucleons estimated using the EPOS model.
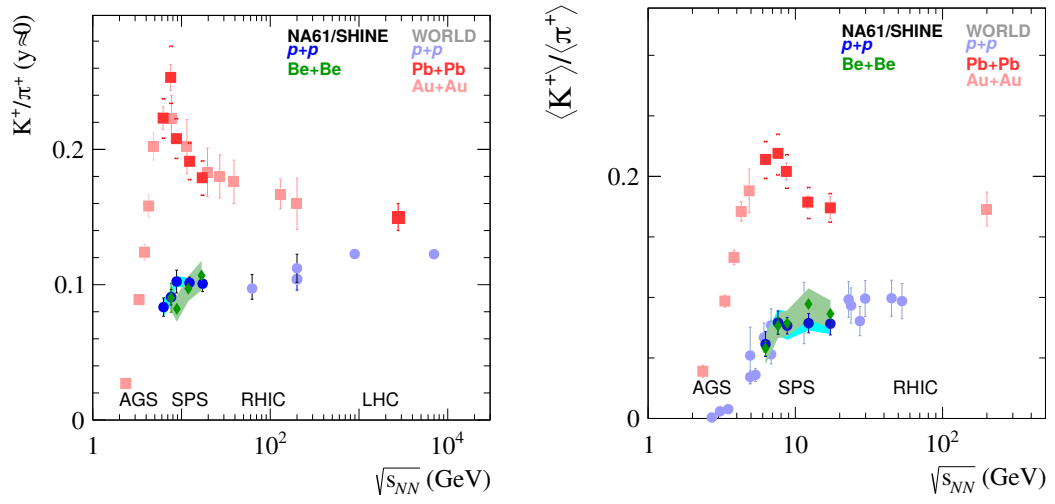
Figure 33: The energy dependence of the K^+/π^+ particle yields ratio at mid-rapidity (*left*) and full acceptance (*right*) for the 20% most *central* Be+Be, *central* Pb+Pb and Au+Au collisions, as well as inelastic *p+p* interactions. Both statistical (vertical bars) and systematic uncertainties (shaded bands) are shown.
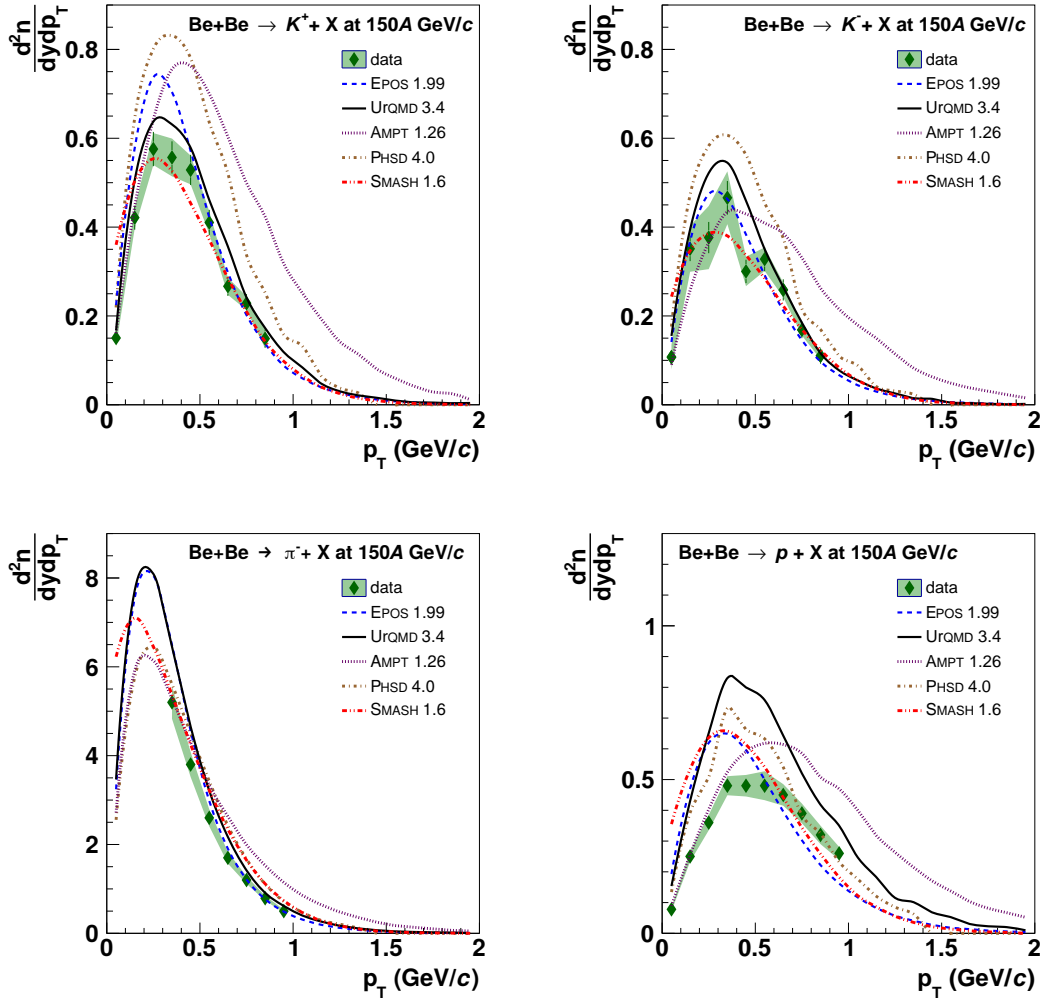
Figure 34: Comparison of the p_T spectra of K^+ (*top-left*), K^- (*top-right*), π^- (*bottom-left*) and p (*bottom-right*) at mid-rapidity for the 20% most *central* Be+Be collisions at 150A GeV/c with models: EPOS 1.99 (blue dashed line), UrQMD 3.4 (black solid line), AMPT 1.26 (violet dotted line), PHSD 4.0 (brown dashed-dotted line) and SMASH 1.6 (red dashed-double dotted line) .
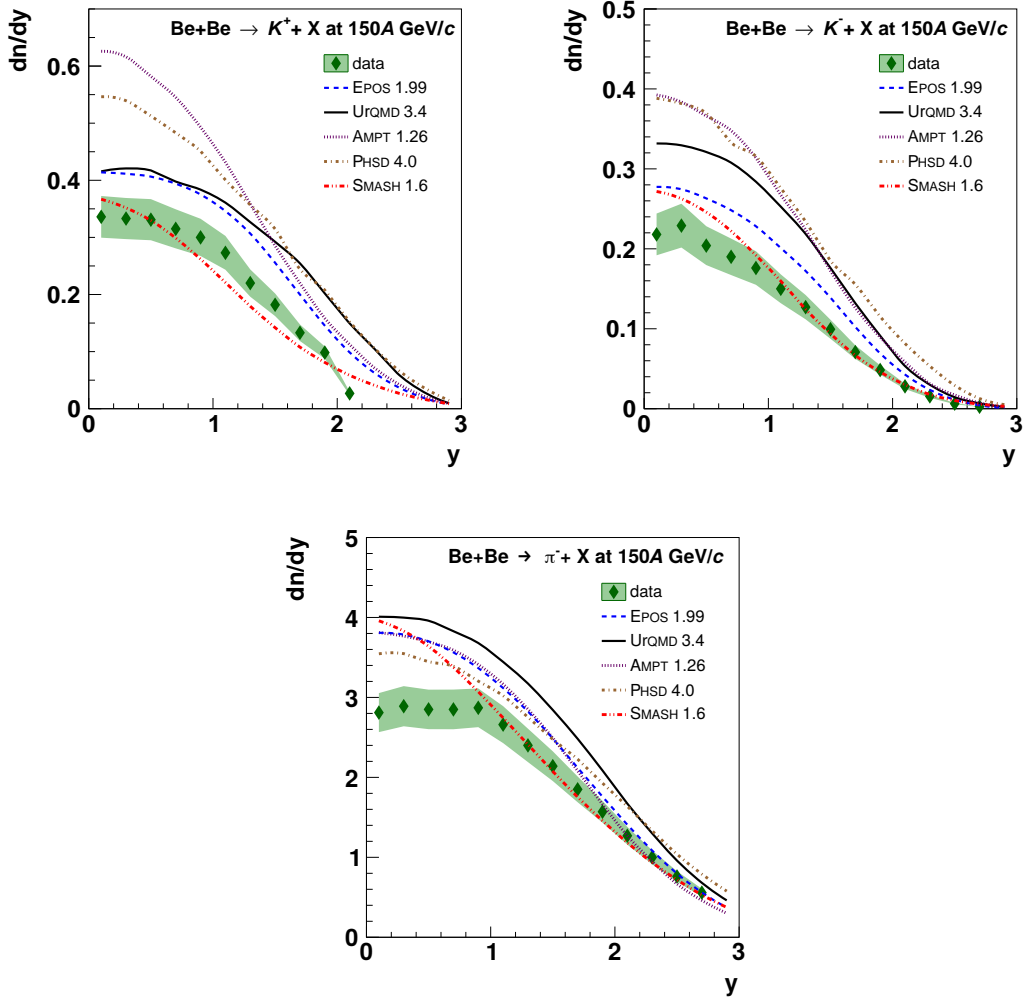
Figure 35: Comparison of the K^+ (*left*), K^- (*right*) and π^- (*bottom*) rapidity spectra for the 20% most *central* Be+Be collisions at $150A$ GeV/c with models: EPOS 1.99 (blue dashed line), UrQMD 3.4 (black solid line), AMPT 1.26 (violet dotted line), PHSD 4.0 (brown dashed-dotted line) and SMASH 1.6 (red dashed-double dotted line) .

Figure 36: Comparison of the energy dependence of the inverse slope parameter T of K^+ (*top-left*), K^- (*top-right*), π^- (*bottom-left*) and p (*bottom-right*) spectra at mid-rapidity for the 20% most *central* Be+Be collisions with models: EPOS 1.99 (blue dashed line), UrQMD 3.4 (black solid line), AMPT 1.26 (violet dotted line), PHSD 4.0 (brown dashed-dotted line) and SMASH 1.6 (red dashed-double dotted line) .
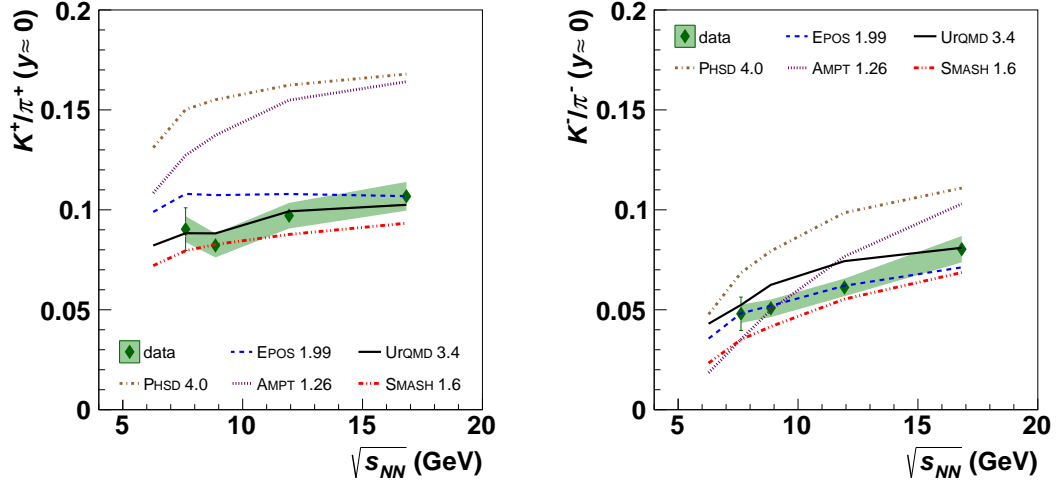
Figure 37: Comparison of the energy dependence of K^+/π^+ (*left*) and K^-/π^- (*right*) yields ratio at mid-rapidity for the 20% most *central* Be+Be collisions with models: EPOS 1.99 (blue dashed line), UrQMD 3.4 (black solid line), AMPT 1.26 (violet dotted line), PHSD 4.0 (brown dashed-dotted line) and SMASH 1.6 (red dashed-double dotted line).
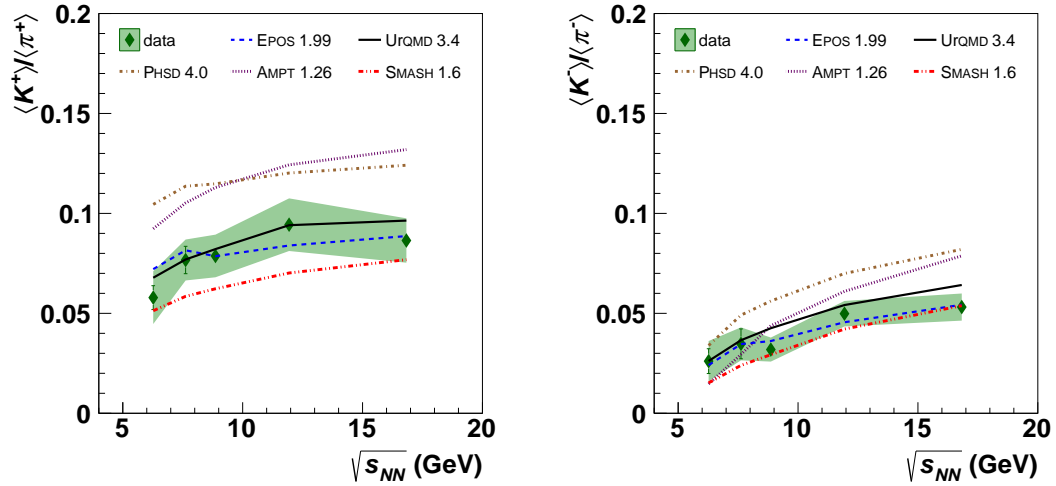
Figure 38: Comparison of the energy dependence of K^+/π^+ (*left*) and K^-/π^- (*right*) mean multiplicities ratio for the 20% most *central* Be+Be collisions with models: EPOS 1.99 (blue dashed line), UrQMD 3.4 (black solid line), AMPT 1.26 (violet dotted line), PHSD 4.0 (brown dashed-dotted line) and SMASH 1.6 (red dashed-double dotted line).

6 Summary and conclusions

This paper reports measurements by the NA61/SHINE experiment at the CERN SPS of spectra and mean multiplicities of $\pi^\pm, K^\pm, p$ and $\bar{p}$ produced in the 20 % most *central* ^{7}Be+^{9}Be collisions at beam momenta of 19A, 30A, 40A, 75A and 150A GeV/c. This is the lightest nucleus-nucleus system investigated in the system size scan of NA61/SHINE. In this program data were also recorded from Ar+Sc, Xe+La and Pb+Pb collisions for which the analysis is ongoing. Results on *central* ^{7}Be+^{9}Be collisions were found to be similar to those from inelastic p+p interactions for shapes of transverse momentum and rapidity spectra as well as the K^+/π^+ ratio. However, particle yields are higher by approximately a factor of four consistent with expectations from the wounded nucleon model. Summarising, neither measurements nor models show indications of a horn structure at low SPS energy for small collision systems in contrast to the results from *central* Pb+Pb interactions, for detailed discussion on possible indications of onset of deconfinement in small systems see Ref. [10].

The results were compared with predictions of the models: EPOS 1.99, UrQMD 3.4, AMPT 1.26, PHSD 4.0 and SMASH 1.6. None of the models reproduces all features of the presented results.

Acknowledgments

References

[1] N. Antoniou *et al.*, [NA61/SHINE Collab.], "Study of hadron production in hadron nucleus and nucleus nucleus collisions at the CERN SPS," tech. rep., CERN, 2006. CERN-SPSC-2006-034.

[2] M. Gazdzicki, M. Gorenstein, and P. Seyboth, "Recent Developments in the Study of Deconfinement in Nucleus-Nucleus Collisions," *Int.J.Mod.Phys.* **E23** (2014) 1430008, arXiv:1404.3567 [nucl-ex].

[3] A. Aduszkiewicz, [NA61/SHINE Collab.], "Beam momentum scan with Pb+Pb collisions," Tech. Rep. CERN-SPSC-2015-038. SPSC-P-330-ADD-8, CERN, Geneva, Oct, 2015. https://cds.cern.ch/record/2059811.

[4] A. Acharya *et al.*, [NA61/SHINE Collab.], "Measurements of π^- production in ^{7}Be+^{9}Be collisions at beam momenta from 19A to 150AGeV/c in the NA61/SHINE experiment at the CERN SPS," arXiv:2008.06277 [nucl-ex].

[5] R. Poberezhnyuk, M. Gazdzicki, and M. Gorenstein, "Statistical Model of the Early Stage of nucleus-nucleus collisions with exact strangeness conservation," *Acta Phys. Polon. B* **46** no. 10, (2015) 1991, arXiv:1502.05650 [nucl-th].

[6] A. Motornenko, V. Begun, V. Vovchenko, M. Gorenstein, and H. Stoecker, "Hadron yields and fluctuations at energies available at the CERN Super Proton Synchrotron: System-size dependence from Pb + Pb to p+p collisions," *Phys. Rev. C* **99** no. 3, (2019) 034909, arXiv:1811.10645 [nucl-th].

[7] M. Gazdzicki and O. Hansen, "Hadron production in nucleon-nucleon collisions at 200-GeV/c: A Compilation," *Nucl.Phys.* **A528** (1991) 754–770.

[8] N. Abgrall *et al.*, [NA61/SHINE Collab.], "Measurement of negatively charged pion spectra in inelastic p+p interactions at p_{lab} = 20, 31, 40, 80 and 158 GeV/c," *Eur.Phys.J.* **C74** (2014) 2794, arXiv:1310.2417 [hep-ex].

[9] A. Aduszkiewicz *et al.*, [NA61/SHINE Collab.], "Measurements of $\pi^\pm$, K$^\pm$, p and p̄ spectra in proton-proton interactions at 20, 31, 40, 80 and 158 GeV/c with the NA61/SHINE spectrometer at the CERN SPS," *Eur. Phys. J.* **C77** no. 10, (2017) 671, arXiv:1705.02467 [nucl-ex].

[10] A. Aduszkiewicz *et al.*, [NA61/SHINE Collab.], "Proton-Proton Interactions and Onset of Deconfinement," *Phys. Rev. C* **102** (2020) 011901, arXiv:1912.10871 [hep-ex].

[11] S. Afanasiev *et al.*, [NA49 Collab.], "Energy dependence of pion and kaon production in central Pb + Pb collisions," *Phys. Rev.* **C66** (2002) 054902.

[12] C. Alt *et al.*, [NA49 Collab.], "Pion and kaon production in central Pb + Pb collisions at 20-A and 30-A-GeV: Evidence for the onset of deconfinement," *Phys. Rev.* **C77** (2008) 024903.

[13] N. Abgrall *et al.*, [NA61 Collab.], "NA61/SHINE facility at the CERN SPS: beams and detector system," *JINST* **9** (2014) P06005, arXiv:1401.4699 [physics.ins-det].

[14] O. Berrig *et al.*, [NA61/SHINE Collab.], "The 2010 test of secondary light ion beams," tech. rep., CERN, 2011. CERN-SPSC-2011-005.

[15] D. Banas, A. Kubala-Kukus, M. Rybczynski, I. Stabrawa, and G. Stefanek, "Influence of target material impurities on physical results in relativistic heavy-ion collisions," *Eur. Phys. J. Plus* **134** no. 1, (2019) 44, arXiv:1808.10377 [nucl-ex].

[16] K. Werner, F.-M. Liu, and T. Pierog, "Parton ladder splitting and the rapidity dependence of transverse momentum spectra in deuteron-gold collisions at RHIC," *Phys.Rev.* **C74** (2006) 044902.

[17] C. F. Brun R., "Geant detector description and simulation tool, cern program library long writeup w5013," 1993. http://wwwasdoc.web.cern.ch/wwwasdoc/geant/geantall.html.

[18] A. Seryakov, [NA61/SHINE Collab.], "PSD acceptance maps for event selection." https://edms.cern.ch/document/1867336/1, 2017. CERN EDMS.

[19] E. Kaptur, [NA61/SHINE Collab.], "PHD thesis: Analysis of collision centrality and negative pion spectra in ^{7}Be+^{9}Be interactions at CERN SPS energy range," 2017. https://edms.cern.ch/document/2004086/1.

[20] A. Bialas, M. Bleszynski, and W. Czyz, "Multiplicity Distributions in Nucleus-Nucleus Collisions at High-Energies," *Nucl. Phys.* **B111** (1976) 461.

[21] W. Broniowski, M. Rybczynski, and P. Bozek, "GLISSANDO: Glauber initial-state simulation and more..," *Comput.Phys.Commun.* **180** (2009) 69.

[22] M. Kuich, [NA61/SHINE Collab.], "PHD thesis: Kaon production in mid-rapidity in Be+Be collisions at the CERN SPS," 2019. `https://edms.cern.ch/document/2150851/1`.

[23] M. van Leeuwen, [NA49 Collab.], "Energy dependence of particle production in nucleus nucleus collisions at the CERN SPS," in *Proceedings, 38th Rencontres de Moriond on QCD and High-Energy Hadronic Interactions.* 2003. `arXiv:nucl-ex/0306004 [nucl-ex]`.

[24] M. van Leeuwen, "A practical guide to de/dx analysis in na49," 2008.

[25] S. Afanasev *et al.*, [NA49 Collab.], "The NA49 large acceptance hadron detector," *Nucl.Instrum.Meth.* **A430** (1999) 210–244.

[26] T. Anticic *et al.*, [NA49 Collab.], "Antideuteron and deuteron production in mid-central Pb+Pb collisions at 158*A* GeV," *Phys. Rev.* **C85** (2012) 044913, `arXiv:1111.2588 [nucl-ex]`.

[27] A. Rustamov and M. Gorenstein, "Identity Method for Moments of Multiplicity Distribution," *Phys.Rev.* **C86** (2012) 044906, `arXiv:1204.6632 [nucl-th]`.

[28] A. Aduszkiewicz *et al.*, [NA61/SHINE Collab.], "Production of Λ -hyperons in inelastic p+p interactions at 158 GeV/*c*," *Eur. Phys. J.* **C76** no. 4, (2016) 198, `arXiv:1510.03720 [hep-ex]`.

[29] R. Hagedorn, "Statistical thermodynamics of strong interactions at high energies. 3. Heavy-pair (quark) production rates," *Nuovo Cim.Suppl.* **6** (1968) 311–354.

[30] W. Broniowski, W. Florkowski, and L. Y. Glozman, "Update of the Hagedorn mass spectrum," *Phys.Rev.* **D70** (2004) 117503, `arXiv:hep-ph/0407290 [hep-ph]`.

[31] T. Pierog, R. Ulrich, and private communication, "EPOS 1.99 version CRMC." See `https://web.ikp.kit.edu/rulrich/crmc/html`, 2018.

[32] M. Gazdzicki and M. I. Gorenstein, "On the early stage of nucleus-nucleus collisions," *Acta Phys.Polon.* **B30** (1999) 2705, `arXiv:hep-ph/9803462 [hep-ph]`.

[33] S. Bass *et al.*, "Microscopic models for ultrarelativistic heavy ion collisions," *Prog.Part.Nucl.Phys.* **41** (1998) 255–369, `arXiv:nucl-th/9803035 [nucl-th]`.

[34] M. Bleicher *et al.*, "Relativistic hadron hadron collisions in the ultrarelativistic quantum molecular dynamics model," *J.Phys.* **G25** (1999) 1859–1896, `arXiv:hep-ph/9909407 [hep-ph]`.

[35] Z.-W. Lin, C. M. Ko, B.-A. Li, B. Zhang, and S. Pal, "Multiphase transport model for relativistic heavy ion collisions," *Phys. Rev. C* **72** (Dec, 2005) 064901.

[36] Z.-W. Lin, "Evolution of transverse flow and effective temperatures in the parton phase from a multiphase transport model," *Phys. Rev. C* **90** (Jul, 2014) 014904.

[37] B. Zhang, C. M. Ko, B.-A. Li, and Z. Lin, "Multiphase transport model for relativistic nuclear collisions," *Phys. Rev. C* **61** (May, 2000) 067901.

[38] W. Cassing and E. L. Bratkovskaya, "Parton transport and hadronization from the dynamical quasiparticle point of view," *Phys. Rev. C* **78** (Sep, 2008) 034919. `https://link.aps.org/doi/10.1103/PhysRevC.78.034919`.

[39] W. Cassing and E. Bratkovskaya, "Parton–hadron–string dynamics: An off-shell transport approach for relativistic energies," *Nuclear Physics A* **831** no. 3, (2009) 215 – 242. `http://www.sciencedirect.com/science/article/pii/S0375947409005995`.

[40] J. Mohs, S. Ryu, and H. Elfner, "Particle Production via Strings and Baryon Stopping within a Hadronic Transport Approach," *J. Phys. G* **47** no. 6, (2020) 065101, `arXiv:1909.05586 [nucl-th]`.

[41] J. Weil, V. Steinberg, J. Staudenmaier, L. G. Pang, D. Oliinychenko, J. Mohs, M. Kretz, T. Kehrenberg, A. Goldschmidt, B. Bäuchle, J. Auvinen, M. Attems, and H. Petersen, "Particle production and equilibrium properties within a new hadron transport approach for heavy-ion collisions," *Phys. Rev. C* **94** (Nov, 2016) 054905. `https://link.aps.org/doi/10.1103/PhysRevC.94.054905`.

[42] M. Gazdzicki, M. Gorenstein, and P. Seyboth, "Onset of deconfinement in nucleus-nucleus collisions: Review for pedestrians and experts," *Acta Phys.Polon.* **B42** (2011) 307–351, arXiv:1006.1765 [hep-ph].

[43] K. Werner, "The hadronic interaction model EPOS," *Nucl. Phys. Proc. Suppl.* **175-176** (2008) 81–87.